GEORG-AUGUST-UNIVERSITÄT
GÖTTINGEN

Fakultät für
Physik

Master's Thesis

Suche nach resonanter und nicht-resonanter Doppelhiggsproduktion im „$hh \rightarrow \gamma\gamma\tau\tau$"-Kanal

Search for resonant and non-resonant di-Higgs production in the '$hh \rightarrow \gamma\gamma\tau\tau$' channel

prepared by

Julian Wollrath

from Hannover

at the II. Physikalisches Institut

Thesis number: II.Physik-UniGö-MSc-2016/07

Thesis period: April 14, 2016 until October 14, 2016

First referee: Prof. Dr. Stan Lai

Second referee: Prof. Dr. Ariane Frey

Abstract

A search is performed for the resonant and non-resonant di-Higgs production in the $hh \to \gamma\gamma\tau_{\text{lep}}\tau_{\text{had}}$ final state using 8.1 fb^{-1} of pp collision data at a centre of mass energy of 13 TeV as recorded by the ATLAS experiment at the Large Hadron Collider in 2015 and the first half of 2016. Additionally, a study is performed to test the expected sensitivity of the ATLAS experiment to observe both resonant and non-resonant di-Higgs production in the $hh \to \gamma\gamma\tau_{\text{lep}}\tau_{\text{had}}$ final state with 30 fb^{-1} pp collision data at a centre-of-mass energy of 13 TeV as it would be recorded with the ATLAS experiment at the Large Hadron Collider. For these, a next-to-leading order effective field theory Monte Carlo was set up for the generation of the resonant di-Higgs production Monte Carlo samples. For 8.1 fb^{-1} of experimental data, no evidence of di-Higgs production is observed and 95 % confidence level upper limits on the production cross sections are set. Also, 95 % confidence level expected upper limits on the production cross sections are set for 30 fb^{-1}. For the non-resonant di-Higgs production for 8.1 fb^{-1} the observed (expected) limit is 42 (40) fb. For 30 fb^{-1} the expected limit is 5.9 fb. For resonant production for a narrow width heavy Higgs boson, cross section limits are set as function of its mass. For 8.1 fb^{-1} the observed (expected) limits range from 42 (39) fb at $m_H = 260\,\text{GeV}$ to 25 (23) fb at $m_H = 1000\,\text{GeV}$. For 30 fb^{-1} the expected limits range from 10.3 fb at $m_H = 260\,\text{GeV}$ to 3.5 fb at $m_H = 1000\,\text{GeV}$.

Keywords: Physics, Master's thesis, Resonant di-Higgs production, Non-resonant di-Higgs production

Contents

1. Introduction

Since the discovery of a new scalar boson in 2012, which so far has been shown to be compatible with a Standard Model (SM) Higgs boson, the investigation of this new particle is an important part of the ATLAS physics programme. Furthermore, many models beyond the Standard Model (BSM) predict new scalar bosons. One class of examples are models containing two Higgs doublets, such as the type II two Higgs doublet model. In this analysis, the $\gamma\gamma\tau\tau$ final state of di-Higgs production in the SM and a type II two Higgs doublet model is investigated.

This thesis describes the the SM, type II two Higgs doublet models and di-Higgs production in chapter 2 and the experimental setup used for data taking in chapter 3. The Monte Carlo samples that are used for signal and background modelling are described in chapter 4. The object and event selections for the $\gamma\gamma\tau\tau$-channel are described in chapter 5 and the final results are presented in chapter 6. Finally, a conclusion of the analysis and an outlook on the prospect of di-Higgs analyses are given in chapter 7.

2. Theoretical Background

2.1. The Standard Model of Particle Physics

The Standard Model of Particle Physics is currently the best description available for elementary spin-half particles (fermions) and integer spin force-carriers (bosons). It is a gauge theory of the gauge group $U(1)_Y \times SU(2)_L \times SU(3)_C$ whose Lagrange density is invariant under local gauge transformations of these groups. Interaction terms arise from these local gauge symmetries. These interaction terms require new fields, which are interpreted as the fields of the gauge bosons and hence are the particles (bosons) mediating the electromagnetic, strong and weak interactions. The gauge symmetries of the Standard Model require all gauge bosons to be massless. However, the W- and Z-bosons are massive. In order to account for this discrepancy, an additional mechanism is necessary, the Brout-Englert-Higgs (BEH) mechanism. This is described in section 2.1.1. The fourth fundamental force, gravity, is not included in the SM.

The weak and the electromagnetic interactions are combined in the group $U(1)_Y \times SU(2)_L$, where $U(1)_Y$ describes the electromagnetic and weak interactions and $SU(2)_L$ describes the weak interaction only. This unification was first done by Glashow, Salam and Weinberg [2–4]. The electromagnetic interaction is mediated by the photon, which couples to electric charge, Q, and does not distinguish between left- (L) and right-handed (R) particles, i. e. particles of different chirality. The weak interaction couples to weak isospin, T, and is mediated by the

Table 2.1.: Gauge bosons of the Standard Model with their properties [1].

Interaction	Gauge boson	Q [e]	Mass [GeV]
Electromagnetic	γ	0	$< 10^{-27}$
Weak	$W^{\pm}$	± 1	80.385(15)
	Z^0	0	91.1876(23)
Strong	g	0	0

Table 2.2.: Fermions of the Standard Model with their properties [1]. Masses marked with † are not from direct measurements but estimated via a mass-independent subtraction scheme.

Generation	Leptons			Quarks		
	flavour	Q [e]	mass [GeV]	flavour	Q [e]	mass [GeV]
1st	ν_e	0	$< 2 \times 10^{-9}$	u	2/3	$2.3^{+0.7}_{-0.5} \times 10^{-3}$†
	e	-1	511×10^{-6}	d	$-1/3$	$4.8^{+0.5}_{-0.3} \times 10^{-3}$†
2nd	ν_μ	0	$< 2 \times 10^{-9}$	c	2/3	$1.275(25)$†
	μ	-1	105.7×10^{-3}	s	$-1/3$	$98(5) \times 10^{-3}$†
3rd	ν_τ	0	$< 2 \times 10^{-9}$	t	2/3	173.2(12)
	τ	-1	1.777	b	$-1/3$	$4.18(3)$†

W- and Z-bosons, with the Z-boson coupling differently to left- and right-handed particles, while the W-bosons only couples to left-handed particles. The charged weak current, i. e. the interaction via exchange of a W-boson, is the only direct mechanism for flavour changes in the SM. The electroweak interaction introduces the hypercharge $Y = 2(Q - T^3)$, with T^3 being the third component of the weak isospin, as a conserved quantity to which all four of these gauge bosons can couple.

The strong interaction is described by the $SU(3)_C$ group. It conserves the colour charge, C, and is mediated by eight massless bosons, the gluons, g. Only gluons and quarks carry colour charge.

The properties of all fundamental gauge bosons are listed in table 2.1.

The fermions of the Standard Model are the leptons and quarks. They can be divided into three generations, with each generation having one left-handed isospin doublet of neutrino or up-type quark ($T^3 = 1/2$) and charged lepton or down-type quark ($T^3 = -1/2$). The right-handed fermions form isospin singlets with $T^3 = 0$. Across the generations, the particle masses increase. Hence new decays become kinematically allowed and not suppressed anymore due to containing particles of their mass shell. Though all other properties are identical across generations as shown in table 2.2.

Neutrinos and electrons are stable particles and up- and down-quark can form stable compound particles, while all the other fermions are unstable and decay quickly. The muon decays into an electron, an electron-neutrino and a muon-neutrino for example. The τ-lepton can decay leptonically or hadronically, as

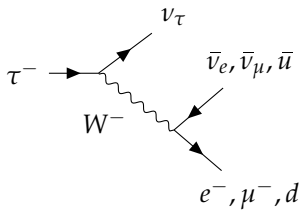

Figure 2.1.: Feynman diagram for the decay of a τ^--lepton. The virtual W-boson can decay either leptonically or hadronically, hence the τ-lepton is considered to decay leptonically or hadronically.

shown in fig. 2.1. When decaying leptonically it decays into a muon or electron and a τ-neutrino plus a electron-neutrino or a muon-neutrino.

Quarks decay weakly into lighter quarks with a branching fraction according to the Cabibbo–Kobayashi–Maskawa matrix. The W-boson from this decay can then decay into quarks or into leptons. In addition to their electric charge, quarks carry colour charge and all but the top-quark cannot be observed as free particles, since they form colourless compound particles, the hadrons which are divided into baryons (containing three quarks) and mesons (containing $q\bar{q}$ pairs). This is called hadonisation. If the energy of a quark is sufficiently high to overcome the binding due to gluon exchange, new quark pairs can be created until the energy of the quarks is not sufficient to do so anymore. Hence, a high energy quark will leave behind a spray of particles called a jet. Due to its huge mass, the top-quark decays before hadronisation.

2.1.1. Electroweak Symmetry Breaking

In the description of the SM so far, the gauge bosons are required to be massless, since masses would no longer allow the Lagrangian to be invariant under symmetry transformations. This contradicts experimental reality, since, as stated in table 2.1, the W- and Z-bosons have non-zero masses. A mechanism was proposed by Robert Brout, Francois Englert, and Peter Higgs that generates the W- and Z-boson masses through spontaneous symmetry breaking [5, 6]. In the BEH mechanism, the Lagrangian remains invariant under its symmetry group

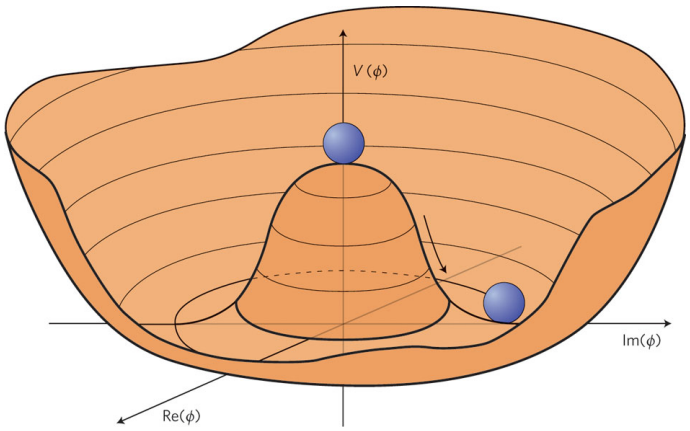

Figure 2.2.: Sketch of the Higgs potential in eq. (2.1.3) with the spontaneous symmetry breaking indicated by a ball going from $V(0)$ to the vacuum state.

but the potential is not symmetric about the ground (vacuum) state. The BEH mechanism adds an additional doublet

$$\Phi = \begin{pmatrix} \phi_1 \\ \phi_2 \end{pmatrix}, \tag{2.1.1}$$

with the complex scalar fields ϕ_1 and ϕ_2. Without loss of generality, one can choose Φ_2 to be minimized in the real direction. One can expand this doublet around the minimum, the vacuum expectation value (vev) v, which gives

$$\Phi = \frac{1}{\sqrt{2}} \begin{pmatrix} 0 \\ v + h \end{pmatrix}, \tag{2.1.2}$$

with h being a scalar field, and

$$V(\Phi) = \mu^2 \Phi^* \Phi + \eta \left| \Phi^* \Phi \right|^2 \supset \frac{1}{2} m_h^2 h^2 + \frac{\eta}{2} m_h h^3 + \frac{\eta}{4} h^4 \tag{2.1.3}$$

is the potential in unitary gauge. This introduces a new scalar boson, the Higgs boson, h, with mass $m_h^2 = \eta v^2/2$ and the vev of the potential $v^2 = -\mu^2/\eta$. In the SM $\mu^2 < 0$ and $\eta > 0$ is required for symmetry breaking, since only then does the potential have minima as shown in fig. 2.2.

Particles acquire their mass due to interaction with this new 'Higgs' field. The masses of the W- and Z-bosons are given by

$$m_W = \frac{1}{2}vg \qquad \text{and} \qquad m_Z = \frac{1}{2}\frac{vg}{\cos\vartheta_W} \tag{2.1.4}$$

with the weak coupling constant g and the weak mixing angle ϑ_W. The masses of the fermions arise from different term in the langrangian and are given by

$$m_f = \frac{v\lambda_f}{\sqrt{2}} \tag{2.1.5}$$

with the Yukawa coupling λ_f of the respective fermion to the Higgs field.

The coupling strength of the Higgs boson to massive bosons is given by

$$\lambda_{hWW} = gm_W \qquad \text{and} \qquad \lambda_{hZZ} = \frac{g}{\cos\vartheta_W}m_Z \tag{2.1.6}$$

and the coupling strength to fermions is given by

$$\lambda_f = \sqrt{2}\frac{m_f}{v}. \tag{2.1.7}$$

Since the photon has no mass, it cannot couple directly to the Higgs boson but only via next-to-leading order processes, e. g. a virtual W-triangle.

The Higgs boson is neutral and CP-even with a mass that is not predicted by theory. In 2012 particle with Higgs-boson-like properties was discovered by the ATLAS and CMS experiments [7, 8]. The current best measurement for its mass is $m_h = 125.09(32)\,\text{GeV}$ [9]. It can decay into bosons and fermions and processes with bosonic and fermionic final states have been investigated, e. g. measurement of $h \to \gamma\gamma$ [10, 11] and evidence for $h \to \tau\tau$ [12, 13]. Branching ratios for the decay into different final states are given in table 2.3. While the W-boson has the strongest coupling to the Higgs boson, the $h \to WW$ process is suppressed, as one W-boson must be off its mass-shell.

2.1.2. Limitations of the Standard Model

The SM is very successful in describing reality, as the comparison of experimental data with theoretical predictions in fig. 2.3 shows: Cross-section measurements with proton-proton collisions at centre-of-mass energies from 7 TeV to 13 TeV of

Table 2.3.: Branching ratio for selected final bosonic and fermionic final states for a $m_h = 125\,\text{GeV}$ SM Higgs boson decay [14].

Final state	Branching ratio [%]
bb	57.7
WW	21.5
$\tau\tau$	6.32
ZZ	2.64
$\gamma\gamma$	0.228

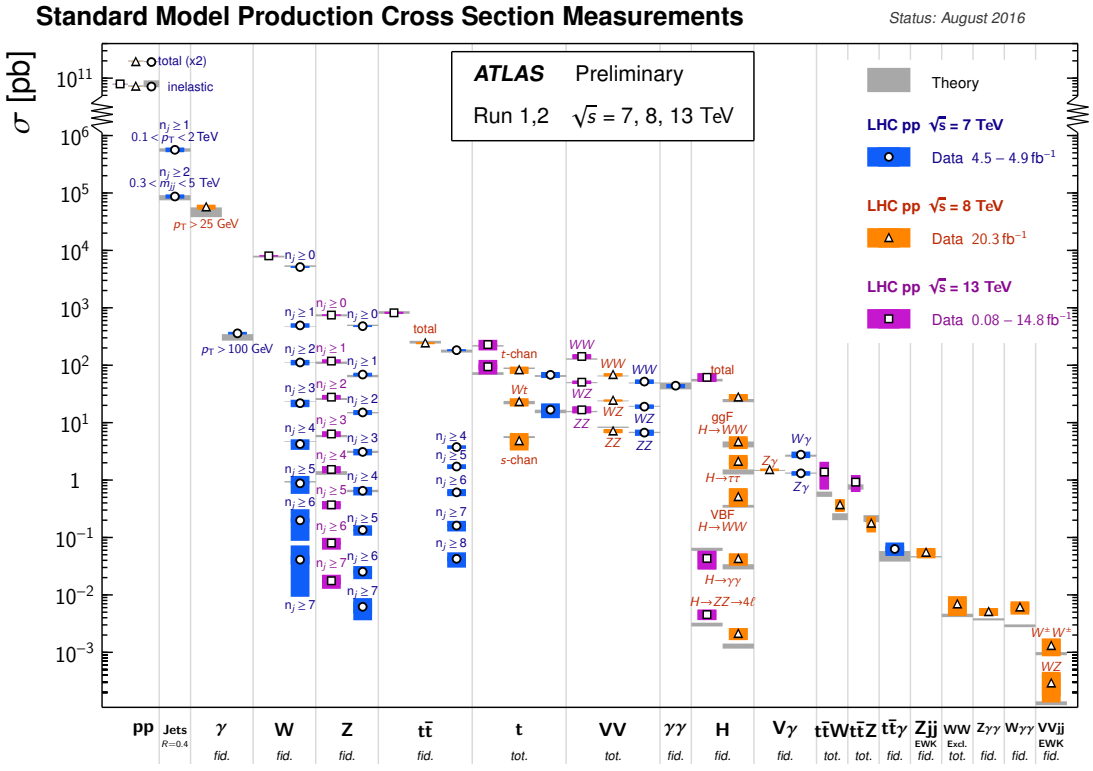

Figure 2.3.: Summary of several Standard Model total and fiducial production cross section measurements, corrected for leptonic branching fractions, compared to the corresponding theoretical expectations. All measurements at different centre-of-mass energies show good agreement with the theoretical predictions [15].

the 19 different processes shown, with several final states investigated, show good agreement with theoretical predictions, while the values for the cross sections span over 14 orders of magnitude.

Despite its success, it also has its limitations. The most notable limitations are given in the following: It considers neutrinos to be massless and therefore fails to describe neutrino oscillations, although they can be included by extending the SM [16]. Furthermore, it is unable to generate a sufficiently large baryon asymmetry of the universe and therefore fails to describe the observed dominance of matter over anti-matter [17]. It also gives no candidates for dark matter, while astrophysical observations give compelling evidence that dark matter exists [18] and it does not include gravity. Many extensions to the SM have in proposed to resolve any number of these issues, for example models containing supersymmetry (SUSY) give explanations for dark matter and a sufficiently large baryon asymmetry.

2.2. Two Higgs Doublet Models

One of the simplest possibilities to extend the SM is to add a second Higgs doublet. Models that do so are called two Higgs doublet models (2HDMs) [19]. These are compelling because they are able to generate a sufficiently large baryon asymmetry by adding additional sources of CP-violation. 2HDMs also appear in other BSM theories such as SUSY and Axion models. In SUSY models, a single Higgs doublet (as in the SM) is unable to give mass simultaneously to up- and down-type quarks. This shortcoming can be resolved by the inclusion of an additional Higgs doublet, which is also required for the cancellation of anomalies. In Axion models, such as the Peccei-Quinn model [20], an additional Higgs doublet is also a required feature.

The Higgs doublets of 2HDMs can be denoted as [21]

$$\Phi_a = \begin{pmatrix} \phi_a^+ \\ \left(v_a + \rho_a + a\eta_a\right)/\sqrt{2} \end{pmatrix}, \tag{2.2.1}$$

with $a = 1, 2$, and the fields ϕ, v, ρ and η. When assuming that CP is conserved and not spontaneously broken and that all odd quartic terms in either of the doublets are eliminated by discrete symmetries, the potential can be written as

$$\begin{aligned} V = \; & m_{11}^2 \Phi_1^\dagger \Phi_1 + m_{22}^2 \Phi_2^\dagger \Phi_2 - m_{12}^2 \left(\Phi_1^\dagger \Phi_2 + \Phi_2^\dagger \Phi_1 \right) + \frac{\lambda_1}{2} \left(\Phi_1^\dagger \Phi_1 \right)^2 \\ & + \frac{\lambda_2}{2} \left(\Phi_2^\dagger \Phi_2 \right)^2 + \lambda_3 \Phi_1^\dagger \Phi_1 \Phi_2^\dagger \Phi_2 + \lambda_4 \Phi_1^\dagger \Phi_2 \Phi_2^\dagger \Phi_1 \\ & + \frac{\lambda_5}{2} \left[\left(\Phi_1^\dagger \Phi_2 \right)^2 + \left(\Phi_2^\dagger \Phi_1 \right)^2 \right]. \end{aligned} \tag{2.2.2}$$

This leads to four scalar bosons: two neutral CP-even, h^0 and H^0 and two charged, $H^\pm$, and one pseudoscalar neutral CP-odd boson, A^0, since three of the fields are needed to give mass to the W and Z. With the minimum

$$\langle \Phi_a \rangle_0 = \frac{1}{\sqrt{2}} \begin{pmatrix} 0 \\ v_a \end{pmatrix} \tag{2.2.3}$$

of the potential, the ratio of the vevs is given by

$$\tan \beta = \frac{v_2}{v_1}, \tag{2.2.4}$$

where β is the angle that diagonalises the mass-squared matrices of $H^\pm$ and A^0. One can redefine the doublets as

$$H_1 = \cos \beta \Phi_1 + \sin \beta \Phi_2 \qquad \text{and} \qquad H_2 = -\sin \beta \Phi_1 + \cos \beta \Phi_2. \tag{2.2.5}$$

For this redefinition, the lower component of H_1 has a real and positive vev $v/\sqrt{2}$ with $v = \sqrt{v_1^2 + v_2^2}$ and H_2 has a vev of zero.

2HDMs can be grouped into different models with similar properties. In this analysis, a generic model of type II will be used. Type II models are CP and flavour conserving [21]. They have a softly broken Z_2 symmetry, meaning that Φ_a transforms as $\Phi_1 \to \Phi_1$ and $\Phi_2 \to -\Phi_2$, and real vacuum expectation values v_i of the Higgs doublets. They feature seven free parameters in total: The masses of the five bosons m_{h^0}, m_{H^0}, m_{A^0} and $m_{H^\pm}$, the mixing angle α among the neutral Higgs bosons, $\tan \beta$ and the soft breaking term of the Z_2 symmetry, m_{12}^2.

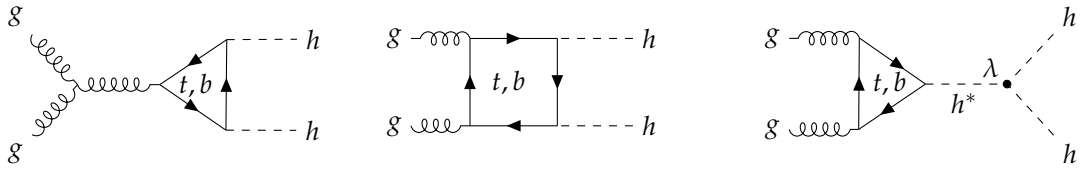

Figure 2.4.: Non-resonant di-Higgs production in the SM via gluon-gluon fusion. On the right, non-resonant di-Higgs production with a trilinear Higgs boson vertex is shown.

2.3. Resonant and Non-resonant di-Higgs Production

A key prediction of the SM is that the h can couple to itself with a coupling strength of $\lambda_{\mathrm{SM}} = \sqrt{\eta/2} m_h$. Trilinear and quartic vertices are possible for the self-coupling, and a measurement of the trilinear coupling in di-Higgs production is in the reach of measurements at the LHC [22] with optimistic predictions giving a precision of $\sim$40 % by the end planned end of LHC [23]. The measurement of the self-coupling is crucial in determining if the scalar boson found in 2012 is the SM or a BSM Higgs boson.

The production of Higgs boson pair happens dominantly via gluon-gluon fusion and is referred to as non-resonant production. This and the other possibilities of di-Higgs production in Born approximation are shown in fig. 2.4.

By measuring the differential cross-section of the non-resonant production, the Higgs boson self-coupling can be measured by looking at the shape of the differential cross-section against kinematic variables such as the p_{T} of the Higgs boson and comparing it against predictions for different coupling strengths as shown in fig. 2.5.

The ATLAS experiment searched for non-resonant Higgs boson pair production in Run I and a limit was set on its cross section as $\sigma^{\mathrm{obs}}_{8\,\mathrm{TeV}}(gg \to hh) \leq 0.69\,\mathrm{pb}$ at a confidence level of 95 % [24]. This is not in reach of the theoretical prediction of the cross section which is $\sigma^{\mathrm{theo}}_{8\,\mathrm{TeV}}(gg \to hh) \approx 10.15\,\mathrm{fb}$ [25]. At 13 TeV, the expected cross section is with $\sigma^{\mathrm{theo}}_{13\,\mathrm{TeV}}(gg \to hh) \approx 33.41\,\mathrm{fb}$ more than thrice as the 8 TeV prediction [25].

In the framework of 2HDM, di-Higgs production is also possible. A neutral heavy Higgs boson, H^0, could decay into a pair of neutral light Higgs bosons, h^0. This is referred to as resonant production. As is the case of the non-resonant production, resonant production also dominantly happens via gluon-gluon fusion. This is shown in fig. 2.6. In the course of this analysis, resonant production also

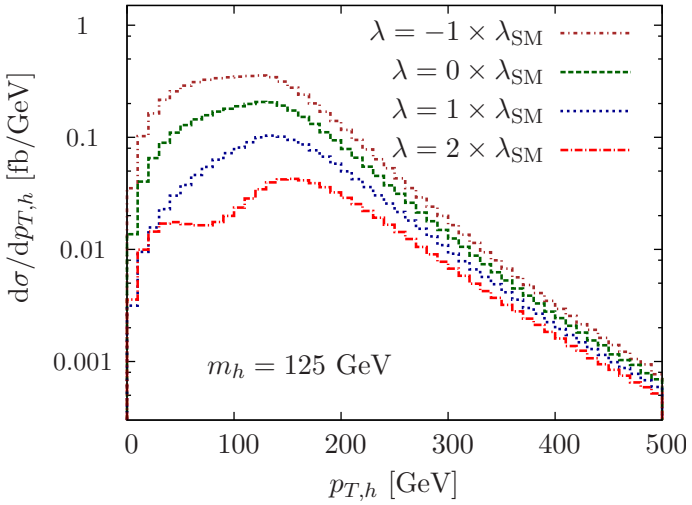

Figure 2.5.: Effect of different Higgs boson self-coupling strengths on the shape of the differential cross-section spectrum against the p_{T} for a Higgs boson with $m_h = 125\,\mathrm{GeV}$ [22].

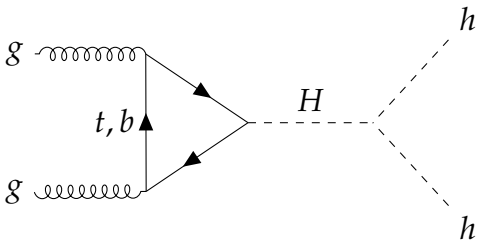

Figure 2.6.: Resonant di-Higgs production via gluon-gluon fusion.

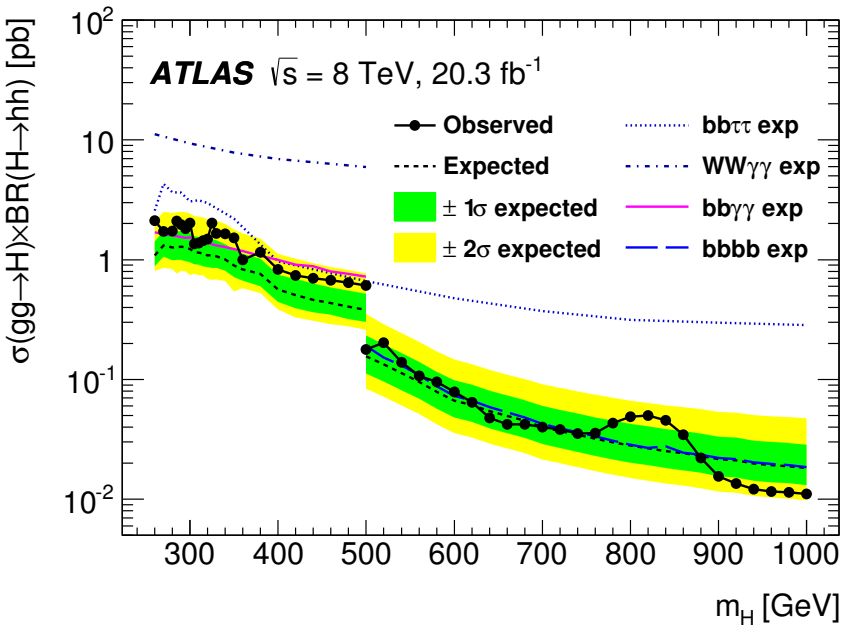

Figure 2.7.: The observed and expected 95 % confidence level upper limits on $\sigma(gg \to H) \times \mathrm{BR}(H \to hh)$ at $\sqrt{s} = 8\,\mathrm{TeV}$ as functions of the heavy Higgs boson mass as measured by ATLAS. The discontinuity at $m_H = 500\,\mathrm{GeV}$ is due to the increased sensitivity due to the additional utilisation of the $4b$ final state [24].

means that the h^0 produced are real, hence it can only occur when $m_{H^0} \geq 2m_{h^0}$. Assuming that the light Higgs bosons are identical to the SM Higgs boson, this process was also searched for at the ATLAS experiment in Run I [24] and limits on the cross section times branching ratio for different masses of H^0 were set as shown in fig. 2.7.

For the searches in [24] the $4b$, $WW\gamma\gamma$, $bb\gamma\gamma$ and $bb\tau\tau$ final states were utilised, since they feature either a high branching ratio (cf. table 2.4) or combine one Higgs boson decaying into a final state with a high branching ratio, e. g. $h \to bb$, with a final state with a signature that is easily separated from background, e. g. $h \to \gamma\gamma$. For the same reason, the $\gamma\gamma\tau\tau$-channel is investigated in this analysis: It combines a final state with a signature that is easily separated from background, $h \to \gamma\gamma$, with a final state that has a reasonable high branching ratio, $h \to \tau\tau$.

Table 2.4.: Branching ratio for the different di-Higgs final states investigated by the ATLAS experiment. Final states marked with † were already investigated in Run I.

Final state	Branching ratio [%]
$bbbb^{\dagger}$	32.49
$bbWW$	25.58
$bb\tau\tau^{\dagger}$	7.08
$WWWW$	5.10
$bb\gamma\gamma^{\dagger}$	0.26
$WW\gamma\gamma^{\dagger}$	0.10
$\gamma\gamma\tau\tau$	0.03

3. The Large Hadron Collider and the ATLAS Detector

3.1. The Large Hadron Collider

The synchrotron-type collider Large Hadron Collider (LHC) [26] is a 27 km in circumference circular proton-proton and heavy ion collider at the European Organization for Nuclear Research (CERN). It is located approximately 100 m below ground at the Franco-Swiss border region near Geneva, Switzerland. It was designed for a centre-of-mass energy of $\sqrt{s} = 14$ TeV and instantaneous luminosity of $5 \times 10^{34}\,\mathrm{cm^{-2}s^{-1}}$. Currently, it is running with a centre-of-mass energy of 13 TeV and an instantaneous luminosity of approximately $10^{34}\,\mathrm{cm^{-2}s^{-1}}$. It has a bunch spacing of 25 ns corresponding to a collision rate of 40 MHz.

A chain of accelerators is used to bring hadrons up to their desired energy before being injected into the LHC for collision. The entire LHC accelerator chain is shown in fig. 3.1. First, H-atoms are ionised by stripping off their electrons. These protons are then accelerated to 50 MeV in the linear accelerator, LINAC 2, and subsequently injected into the Booster, where they are accelerated to 1.4 GeV. From there, they are injected into the Proton Synchrotron (PS) and accelerated to 25 GeV. Then they are passed on into the Super Proton Synchrotron (SPS) where they are accelerated to 450 GeV, the minimum injection energy for the LHC, and only then are injected into the LHC. In the LHC, they are accelerated to their final collision energy of 6.5 TeV, giving a centre of mass energy of 13 TeV. Data and Monte Carlo samples for these proton-proton collisions are used in this analysis.

In case of heavy ions, the acceleration chain differs slightly from the one described for protons: The particles are not accelerated by LINAC 2 and the Booster but instead are accelerated by the linear accelerator LINAC 3 and the Low Energy Ion Ring (LEIR) before getting injected into the PS.

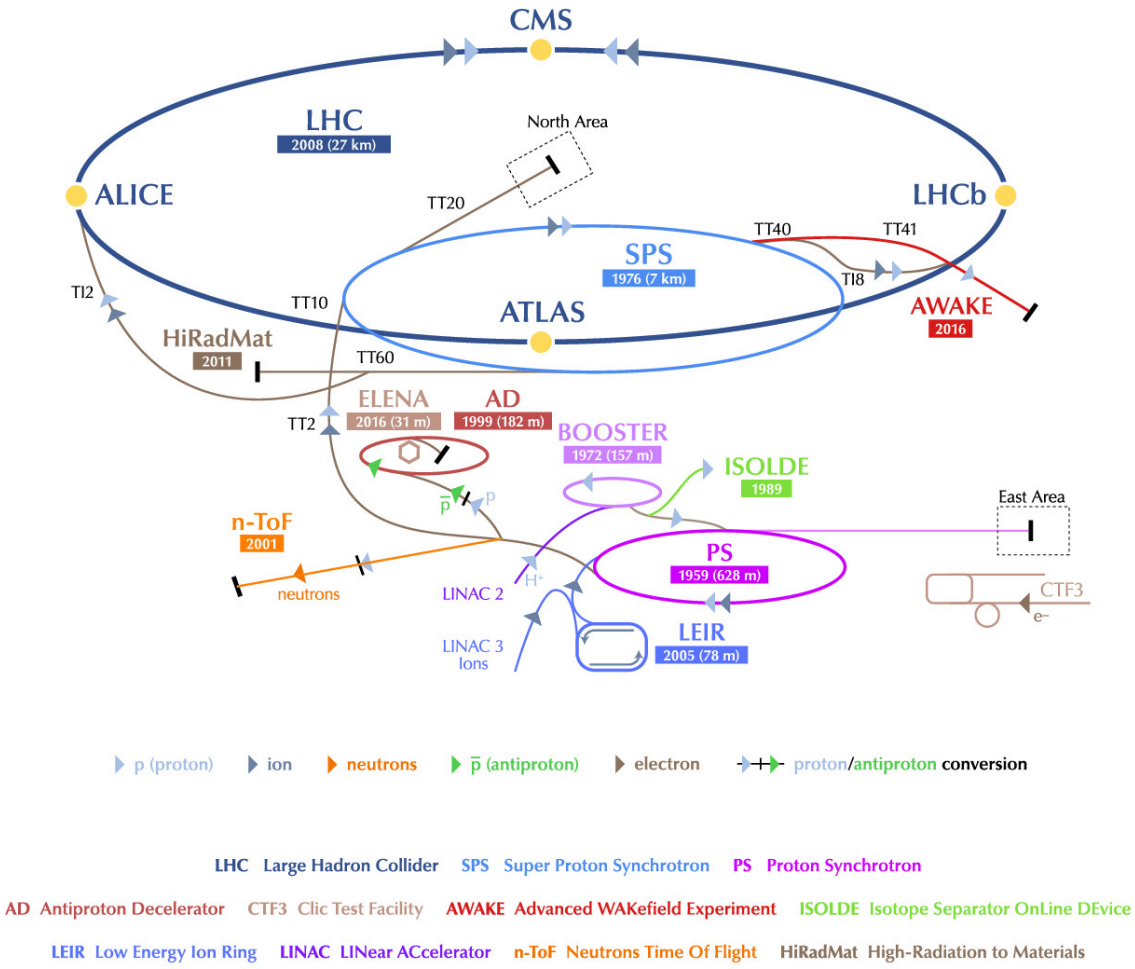

Figure 3.1.: The CERN accelerator complex [27].

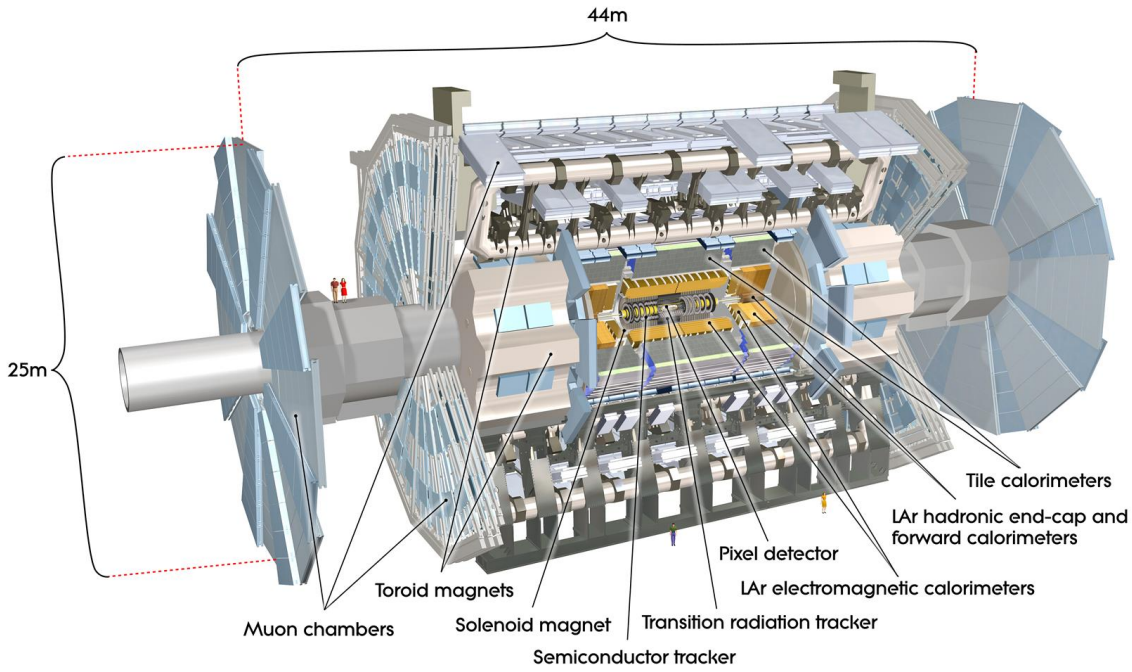

Figure 3.2.: Schema of the ATLAS detector [35].

For the acceleration in the LHC, high frequency cavities are employed. The beam is bent such that it follows the circular beam pipe via 1232 superconducting dipole magnets providing a magnetic field of 8.33 T each. Two beams circulate the LHC in opposite direction. The protons are accelerated in bunches containing $\sim 10^{11}$ protons and collided at four different collision points at which the experiments are located. In Run II, 2808 of these bunches are filled into the LHC with a spacing of 25 ns.

The LHC hosts four large experiments, the two multi-purpose experiments: A Toroidal LHC Apparatus (ATLAS) [28] and the Compact Muon Spectrometer (CMS) [29]; as well as the more specialised experiments LHCb [30] and A Large Ion Collider Experiment (ALICE) [31]. Their positions are also indicated in fig. 3.1. Furthermore, it hosts three small experiments, the Total Elastic and Diffractive Cross Section Measurement (TOTEM) [32], LHC forward (LHCf) [33] and the Monopole and Exotics Detector at the LHC (MoEDAL) [34].

Table 3.1.: Requirements for resolution and pseudorapidity coverage of the different sub-detector systems [28].

Sub-detector system	Required resolution	$\lvert\eta\rvert$ coverage
Inner detector	$\sigma_{p_T}/p_T = 0.05\,\% p_T \oplus 1\,\%$	≤ 2.5
EM calorimeter	$\sigma_E/E = 10\,\%/\sqrt{E} \oplus 0.7\,\%$	≤ 3.2
Tile and end-cap HCal	$\sigma_E/E = 50\,\%/\sqrt{E} \oplus 3\,\%$	≤ 3.2
Forward HCal	$\sigma_E/E = 100\,\%/\sqrt{E} \oplus 10\,\%$	$3.1 < \lvert\eta\rvert < 4.9$
Muon spectrometer	$\sigma_{p_T}/p_T = 0.05\,\%$ at $p_T = 1\,\text{TeV}$	≤ 2.7

3.2. The ATLAS Experiment

The ATLAS experiment is one of the two multi-purpose experiments at the LHC. Weighing around 7000 tonnes with a height of 25 m and a length of 45 m it is the largest detector of its kind. It has a cylindrical structure and is built symmetrically around the collision point (see fig. 3.2). It is designed to be as hermetic around the point of collision as possible. In analysis of the experimental data, a right handed coordinate system is used such that the $+x$ direction points towards the centre of the LHC and the $+y$ direction points upwards. The $+z$ direction follows accordingly along the beamline. In practice, a cylindrical coordinate system with $z = 0$ at the point of collision is used. The azimuthal angle, ϕ, is measured in the plane transverse to the beam-pipe with $\phi = 0$ pointing towards the centre of the LHC ring. The polar angle, θ, is measured from the z-axis towards the azimuthal plane. Instead of the polar angle, the pseudorapidity $\eta = -\ln\left(\tan\frac{\theta}{2}\right)$ is used, since differences in η are approximately Lorentz invariant under boosts along the longitudinal axis. The momentum perpendicular to the z-axis, the transverse momentum, p_T, is often used to describe the kinematics of measured particles.

The ATLAS detector is made from several sub-detector systems, which all cover the range of 4π in ϕ but differ in their coverage with respect to pseudorapidity as shown in table 3.1. The designed resolution for the different sub-detector systems is also shown in table 3.1.

All of the detector components, except the calorimeters, are covered by the magnetic field of the magnet system [36], such that charge and momentum of charged particles can be measured by their deflection in the magnetic field. This field is created by three open air toroids and and a central solenoid (see fig. 3.2). The toroids magnetic field is designed to be mostly orthogonal to the particle

trajectory and to extend the η-coverage of the muon spectrometer by deflecting muons into it, while not negatively impacting the performance of the calorimeters. The utilized magnets are superconducting magnets, cooled to 4.5 K using liquid helium.

The central solenoid deflects charged particles in the ϕ plane, due to its field being parallel to the beam axis. It provides a magnetic field of 2 T with a constant strength along the radial direction and decreasing with the distance in z direction from the interaction point.

The end-cap and barrel toroids provide fields of 3.9 T and 4.1 T respectively, which deflect charged particles in the η plane.

The inner detector is built nearest to the collision point. It is built to detect charged particles with hit efficiency close to 100 %. From inward to outward, it consists of the Pixel Detector, the Semiconductor Tracker (SCT) and a gaseous detector, the Transition Radiation Tracker (TRT) [37, 38].

The Pixel Detector consists of four layers of hybrid silicon pixel detectors. The innermost layer, the Insertable B-Layer (IBL) [39], was newly added during the shutdown of the LHC between Run I and Run II to improve tracking, vertexing and b-tagging at high luminosities. To achieve high tracking resolutions the Pixel Detector uses a pixel size of 50 µm $\times$ 400 µm.

The SCT also consist of four cylindrical layers around the beam pipe. Furthermore there are nine layers in each forward and backward direction perpendicular to the beam pipe (end-cap layers). These layers consist of silicon strip detectors, such that two-dimensional tracking information can be obtained by combining information of several layers, which are rotated by an angle of 40 mrad to each other.

The TRT is an ensemble of straw tube gaseous detectors that covers both the barrel and the end caps (forward and backward region) up to $|\eta| \sim 2$. They are especially suited to detect electrons. It is used to identify photons from transition radiation processes and to differentiate between electrons and other charged particles.

The inner detector is surrounded by the calorimeters where the energy of particles is measured by stopping them in the calorimeter volume. The ATLAS calorimeter system is divided into an electromagnetic and a hadronic calorimeter (HCal) [28, 40, 41].

The electromagnetic calorimeter is a sampling liquid argon (LAr) calorimeter with lead as absorbing material. Electron and photon showers, formed by bremsstrahlung and electron-positron pair creation, are stopped in it and their energy is measured by reading out the signal created by the ionisation of the liquid argon.

The hadronic calorimeter is located just outside the electromagnetic calorimeter. It is built out of three different technologies each being used in a different detector region, due to having different requirements on radiation resistance and performance in these regions.

In the most forward region, the forward calorimeter is located. It is built out of tungsten absorbers in a copper matrix with liquid argon as active material. The hadronic end-cap calorimeter also uses liquid argon as active material but uses copper plates as absorbers instead of tungsten, while the tile calorimeter is built out of iron absorbers and plastic scintillators as active material. The plastic scintillators are read out of by photomultipliers.

The outermost sub-detector of the ATLAS detector is the muon spectrometer [42]. Only muons and particles invisible to the detector such as neutrinos are not stopped by the calorimeters and reach the muon spectrometer. It is able to provide precise measurements of muon p_{T} up to approximately 3 TeV and consists of four different types of gaseous proportional chambers.

With a collision rate of 40 MHz, it is not possible to record every event detected by ATLAS. Hence, the data is filtered before recording by two stages of triggers, the hardware based level 1 (L1) trigger, and the software base level high-level trigger (HLT) [43]. The L1 trigger utilises information from the small wheel, which is located just in front the end-cap toroids, the muon system and parts of the calorimeter. The L1 trigger reduces the apparent rate to 40 kHz to 100 kHz by identifying e, μ, γ, jets and neutrinos by missing transverse energy, $E_{\mathrm{T}}^{\mathrm{miss}}$, and requiring a specific combination of them, i. e. having at least two photons in the event. The remaining events are filtered by the HLT, which refines the selection of the L1 trigger further by applying sharper cuts on p_{T} and $E_{\mathrm{T}}^{\mathrm{miss}}$. It also performs speed optimised full event reconstruction and analysis and cuts down the apparent event rate even more by requiring specific signatures of physics processes, i. e. two photons with high p_{T}.

All in all, this brings the apparent event rate down to approximately 1 kHz. These remaining events are stored to disk for further analysis.

4. Monte Carlo Samples

For modelling the signal and the $h \to \gamma\gamma$ background processes, Monte Carlo (MC) samples are used. After generation with the respective MC generators, all events are passed through a GEANT 4 [44] simulation of the ATLAS detector and reconstructed using the same methods as used for collision data. If two generators are mentioned for a sample, the matrix element was generated by the first generator and this was then passed to the second generator for showering, i. e. decaying the final state particles on matrix element level further while considering hadronisation and the subsequent decays of the hadrons.

4.1. Background Modelling

For modelling the backgrounds that include a Higgs boson, MC samples for gluon-gluon fusion (ggF), vector boson fusion (VBF) and Higgsstrahlung (Vh), i. e. a vector boson radiating a Higgs boson, with the Higgs boson decaying to a pair of photons were used. All samples assume $m_h = 125\,\text{GeV}$. The ggF and VBF samples are produced with Powheg+Pythia8 [45, 46] with the CT10 [47] parton density functions (PDF) and the AZNLOCTEQ6L1 PDF tune [48] for Pythia8. The Vh samples are produced with Pythia8 with the NNPDF23LO [49] PDF and

Table 4.1.: MC samples used for the $h \to \gamma\gamma$ background modelling with the cross-section times branching ratio for $h \to \gamma\gamma$ of the processes and the number of events available in the respective sample.

Process	$\sigma \times \text{BR}(h \to \gamma\gamma)$ [pb]	Number of generated events	Effective $\int \mathcal{L}\,\mathrm{d}t$ [ab^{-1}]
ggF	0.1	1 919 000	19.19
VBF	8.58×10^{-3}	984 000	114.7
Wh	3.12×10^{-3}	246 200	78.91
Zh	2.00×10^{-3}	247 800	123.9

Table 4.2.: Cross-section times branching ratio of $hh \to \gamma\gamma\tau_{\text{lep}}\tau_{\text{had}}$ and number of events in the samples for the resonant signal.

Mass point [GeV]	$\sigma \times \text{BR}(hh \to \gamma\gamma\tau_{\text{lep}}\tau_{\text{had}})$ [ab]	Number of generated events	Effective $\int \mathcal{L}\,\mathrm{d}t$ [zb^{-1}]
260	462	100 000	0.22
300	462	97 000	0.21
400	123	97 000	0.79
500	129	100 000	0.77
600	77.1	99 000	1.28
700	13.9	98 000	7.07
750	13.7	94 000	6.86
800	67.8	98 000	1.45
900	17.9	99 000	5.54
1000	13.9	89 000	6.42

the A14NNPDF23LO PDF tune [50]. The properties of the samples are shown in table 4.1.

4.2. Signal Modelling

4.2.1. Non-resonant Signal Modelling

For the non-resonant signal, a next-to-leading-order (NLO) MC ggF sample is used, since ggF is the dominant production mode for di-Higgs production. The sample is produced with MadGraph5_aMC@NLO+Herwig++ [51, 52] using the CT10ME [47] parton distribution functions. The sample consists of 99 000 events which corresponds to $\int \mathcal{L}\,\mathrm{d}t = 22.5\,\text{zb}^{-1}$. The theory prediction for non-resonant di-Higgs production at $\sqrt{s} = 13\,\text{TeV}$ is $\sigma = 33.41\,\text{fb}$ [25], hence $\sigma \times \text{BR}(h \to \gamma\gamma\tau_{\text{lep}}\tau_{\text{had}}) = 4.395\,\text{ab}$ is used as prediction in this analysis.

4.2.2. Resonant Signal Modelling

The resonant signal was produced with MadGraph5_aMC@NLO+Herwig++ using a NLO effective field theory approach [53] for MadGraph5_aMC@NLO and the CT10 parton distribution functions. Only ggF is considered, since this is expected to be the dominant production mode for resonant di-Higgs production at the LHC. It is assumed that the heavy Higgs boson only decays into light Higgs

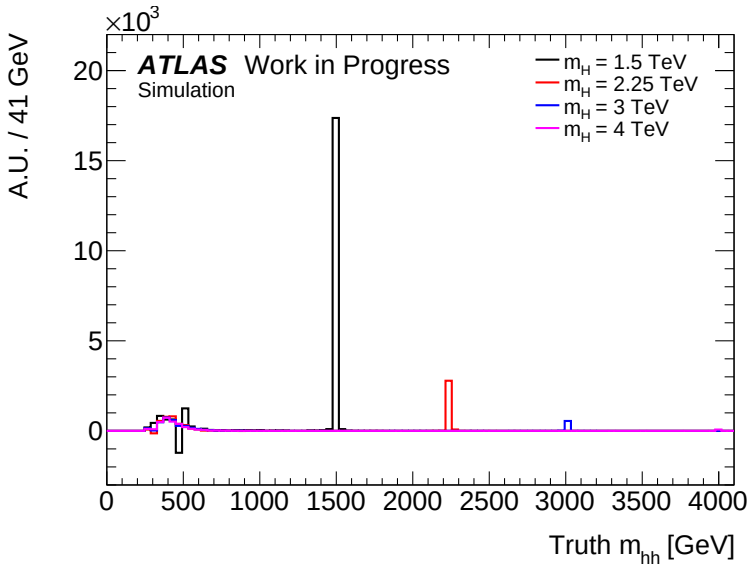

Figure 4.1.: Mass of the di-Higgs system on generator level without showering and detector simulation for different mass points with $\Gamma_H = 1\,\text{GeV}$. Resonance peaks at the respective m_H and a mass independent contribution in the low mass tail are visible.

bosons and that the light Higgs boson, h^0, is identical to the SM Higgs boson. Samples have been produced for ten different mass points as shown in table 4.2. The heavy Higgs boson was chosen to have a decay width of $\Gamma_H = 1\,\text{MeV}$. The cross-section times branching ratio for the different mass points were chosen so, that they are just below the exclusion limits from Run I as given in fig. 2.7. Their values are given in table 4.2 as well as the number of events per sample.

4.3. Validation of the Resonant Signal Modelling

Since the resonant signal model was newly integrated into Athena[1] it had to be validated. This was first done on generator truth level without showering and detector simulation. The di-Higgs mass spectrum (see fig. 4.1) showed an aggregation of events in the low mass tail above the di-Higgs generation threshold of $2m_h$ independent of the mass of the heavy Higgs boson. Further investigation showed that the contribution in the low mass tail is dependant on the decay width of the heavy Higgs boson. This is shown in fig. 4.2. The model used for generation also includes the possibility for the heavy Higgs boson being off its

[1] Athena is the software framework used in the ATLAS experiment.

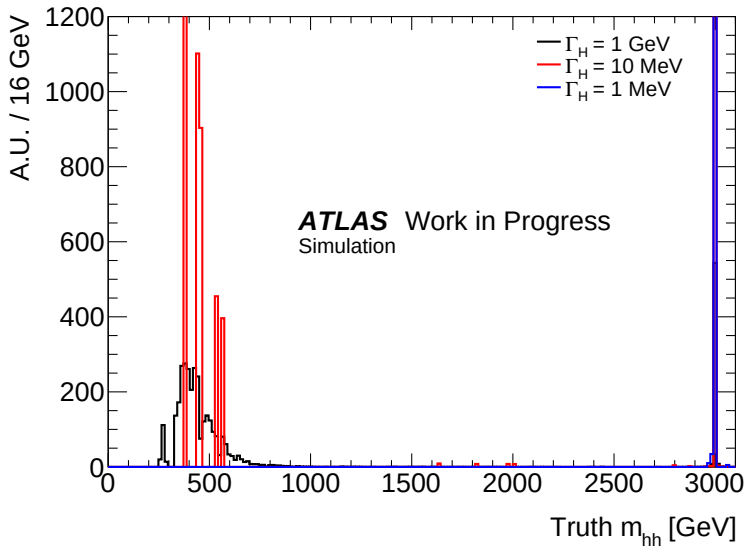

Figure 4.2.: Mass of the di-Higgs system on generator level without showering and detector simulation for different decay widths with $m_H = 3\,\text{TeV}$. For each decay width 100 000 events were simulated. A smaller width leads to a smaller number of events in the low mass tail. Due to having less events in the low mass tail for $\Gamma_H = 10\,\text{GeV}$ than for $\Gamma_H = 1\,\text{GeV}$, the MC generator assigns them a bigger weight to account for the lower statistics.

mass shell and the behaviour shown in the low mass tail is as expected from contributions from a decay of a virtual heavy Higgs boson, i. e., it is less likely to occur at smaller decay widths. This is due to the fact, that according to the PDFs it is more likely for partons to carry a low momentum fraction which results in a smaller effective collision energy $\sqrt{\hat{s}}$ and therefore lower m_{hh} are preferred. Hence, the smaller the decay width of the heavy Higgs boson is, the less likely it is, that it can be produced off its mass shell and therefore, the contribution in the low mass tail is smaller for small decay widths of the heavy Higgs boson. Since the heavy Higgs boson analyses of ATLAS search for a resonance, it is important to have high statistics for the resonant peak, since the low mass distribution would not contribute to a discovery or mass measurement. Furthermore, there is no model independent theoretical prediction of the decay width of the heavy Higgs boson and therefore, it was decided to use a small width ($\Gamma_H = 1\,\text{MeV}$) approximation to eliminate the events in the low mass tail and enhance the statistics in the resonant peak. Since even $\Gamma_H = 1\,\text{GeV}$ is below the expected mass resolution of the ATLAS experiment, the decay width can be chosen to be arbitrarily small without affecting the detection sensibility.

After this first validation step, the decay of the light Higgs bosons was added to the sample generation. This was validated by looking at *inter alia* p_{T} distributions and reconstructing the light and heavy Higgs boson resonances. p_{T} distributions for the $m_H = 260\,\mathrm{GeV}$ resonant production are shown in fig. 4.3. Additional validation plots for the $m_H = 260\,\mathrm{GeV}$ and the $m_H = 600\,\mathrm{GeV}$ resonant production are shown in appendix A. All distributions exhibit the expected behaviour with particles masses being as expected (e. g. m_H as it was requested) and p_{T} distribution showing the expected shape.

With the validation, scripts to integrate the sample generations into the ATLAS software framework, called job options, were written for the $4b$, $bbWW$, $bb\tau\tau$, $4W$, $bb\gamma\gamma$, $WW\gamma\gamma$ and $\gamma\gamma\tau\tau$ final states, which will be investigated by ATLAS in run II. The common part of the job options and the job option for the $m_H = 260\,\mathrm{GeV}$ mass point for the $\gamma\gamma\tau_{\mathrm{lep}}\tau_{\mathrm{had}}$-channel are shown in appendix D.

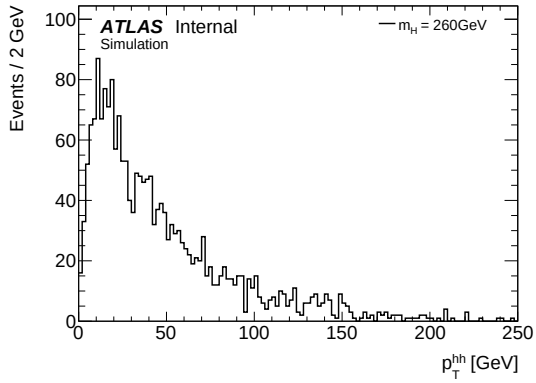

(a) di-Higgs boson system p_{T}

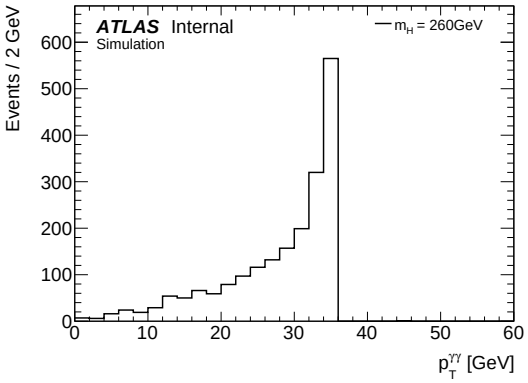

(b) di-photon system p_{T}

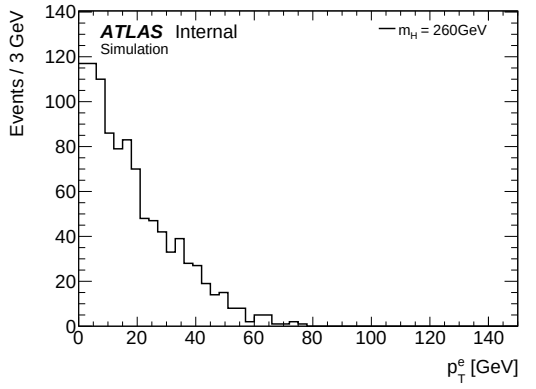

(c) electron p_{T}

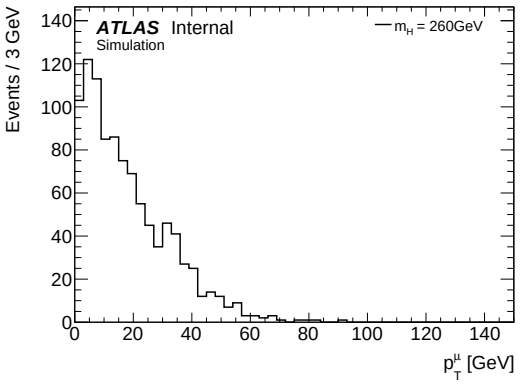

(d) muon p_{T}

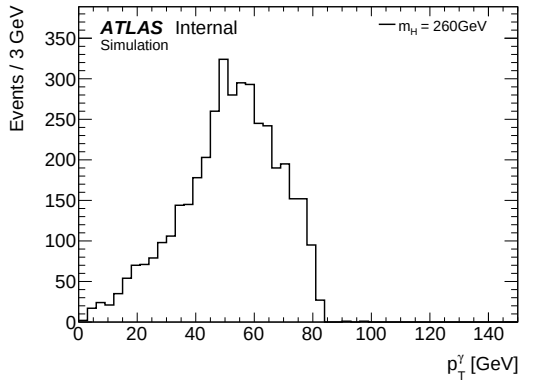

(e) photon p_{T}

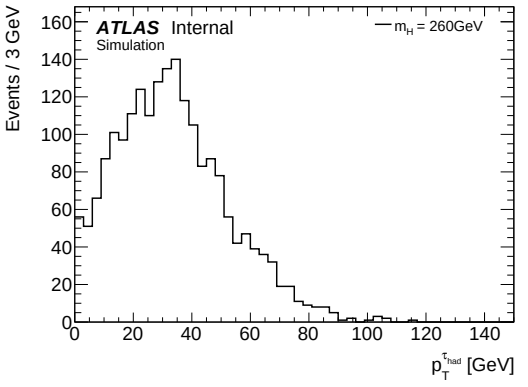

(f) τ_{had} p_{T}

Figure 4.3.: p_{T}-distributions on generator truth level for the resonant production for $m_H = 260\,\mathrm{GeV}$ for a validation sample containing 2000 events. All distributions show the expected behaviour.

5. The $hh \rightarrow \gamma\gamma\tau\tau$-process

The final state investigated in this analysis is the $hh \rightarrow \gamma\gamma\tau\tau$-channel with one τ-lepton decaying leptonically into a muon or an electron plus neutrinos and the other τ-lepton decaying hadronically. The branching ratio for leptonically decaying τ-leptons is 35.24 % [1]. When decaying hadronically it decays into a τ-neutrino and a charge conserving amount of light hadrons, where 1-prong decays (containing one charged particle, e. g. a charged pion) and 3-prong decays (containing three charged particles) are the most common final states. This branching ratio is 64.76 % [1].

This final state is chosen since the leptonically decaying τ-lepton (τ_{lep}) gives one τ-lepton, which is easily separable from background, compared to the hadronically decaying τ-lepton (τ_{had}). The inclusive $\gamma\gamma\tau\tau$ final state has a branching ratio of 0.034 %, with $\sim$ 45.6 % of that being events with a $\gamma\gamma\tau_{\text{lep}}\tau_{\text{had}}$ final state, resulting in a final branching ratio for $\gamma\gamma\tau_{\text{lep}}\tau_{\text{had}}$ of 0.013 %.

5.1. Event Topology

In the $hh \rightarrow \gamma\gamma\tau\tau$-process, due to momentum conservation, the two (light) Higgs bosons are dominantly produced back-to-back in the rest-frame of the initial

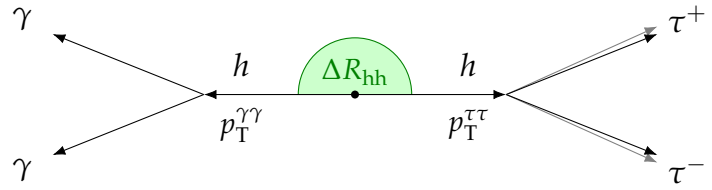

Figure 5.1.: Sketch of the event topology. The (heavy) Higgs boson decays into a pair of Higgs bosons, which move away left and right from the interaction point in the centre. They then subsequently decay into two photons and two τ-leptons respectively. The τ-leptons cannot be detected but their decay products (black) without the neutrinos (grey) are detected.

decaying (heavy) Higgs boson as shown in fig. 5.1. Hence, kinematic variables that highlight this topology will be investigated, e. g. the angular separation between the two reconstructed Higgs bosons ΔR_{hh} and the p_{T}-balance between the $\gamma\gamma$- and $\tau\tau$-systems. For this, events should contain two reconstructed photons, one reconstructed τ_{lep} and one reconstructed τ_{had}.

5.2. Object Definitions

The events recorded by the detector are reconstructed offline by combining the signals recorded in the sub-detectors into different objects, which correspond to physical particles and missing transverse energy respectively.

5.2.1. Leptons

Electron candidates are reconstructed by matching tracks in the inner detector to clusters of energy deposits in the electromagnetic calorimeter. They are identified using a cut-based selection to discriminate between prompt electrons and electrons from background processes, e. g. electrons from pair production and from hadronic jets misidentified as electrons [54]. Three standard selections are provided by the tools used in ATLAS: the loose, medium and tight working points. Here, the medium working point is used, which has an efficiency $\sim$90 % for $p_{\mathrm{T}} > 20\,\mathrm{GeV}$ electrons as measured using electrons from $Z \to ee$ decays [54]. Electron candidates are required to have $p_{\mathrm{T}} > 15\,\mathrm{GeV}$ and to not lie in the transition region $1.37 < |\eta| < 1.52$ between the barrel and end-cap calorimeters. They are also required to not lie within $\Delta R = 0.4$ of a photon candidate and $\Delta R = 0.2$ of a τ_{had} candidate.

Muon candidates are reconstructed by matching tracks in the muon spectrometer to tracks in the inner detector. Track pairs with a small ΔR are identified and a track is fitted to the tracks in both the muon spectrometer and the inner detector [55]. Four standard selections are provided by the tools used in ATLAS: the loose, medium, tight and high-p_{T} selections. In this analysis, the loose selection is used, which is designed for maximal reconstruction efficiency while still providing muons tracks of good quality. For muons with $p_{\mathrm{T}} < 20\,\mathrm{GeV}$ it has a efficiency of $\sim$96 %, for higher p_{T}-muons it has an efficiency of $\sim$98 % [55]. Muon candidates are also required to have $p_{\mathrm{T}} > 12\,\mathrm{GeV}$ and $|\eta| < 2.5$.

There are two kinds of τ-lepton candidates: Candidates for a τ_{lep} and candidates for a τ_{had}. For the latter ones, energy deposits in the calorimeters are required to have $|\eta| < 2.5$ excluding $1.37 < |\eta| < 1.52$ are clustered using the anti-k_{T} algorithm [56] with $R = 0.4$. Each τ_{had}-candidate is associated with tracks that lie within $\Delta R < 0.2$ of the axis of the seed of the jet, if they fulfil specific quality criteria. As there are many reconstructed primary vertices in a given event, the primary vertex of the τ_{had}-candidate is the vertex with the highest sum of p_{T} of tracks associated to the τ_{had}-candidate [57]. Furthermore, the τ_{had} candidate has to have at least one prong (i. e. charged track) and $p_{\text{T}} > 18\,\text{GeV}$.

For identification of τ_{had}'s a boosted decision tree, utilising additional discriminating variables, is trained and three different working points are provided by the tools used in ATLAS, the loose, medium and tight working points. In this analysis the medium working point is used, which has a signal efficiency of 0.55 for one prong and 0.4 for three prong τ_{had}'s [57].

τ_{lep}-candidates are reconstructed as muons or electrons.

τ_{lep}- and τ_{had}-candidates only include the detector visible fraction of the τ-lepton four-vector. The neutrinos occurring in the τ-decay will not be detected but accounted for in the missing transverse energy (cf. section 5.2.3).

5.2.2. Photons

Photons can be classified into two categories: converted and unconverted photons. Converted photons are photons that have undergone pair creation (i. e. $\gamma \to e^+e^-$) in the inner detector, they are reconstructed in a similar fashion to electrons: At least one track from a vertex inside the inner detector is matched to a cluster of energy deposits in the electromagnetic calorimeter. Matched in this case means, that the photon's impact point after extrapolation from its last measurement to the calorimeter second sampling is within (η, ϕ) range of $\eta = \phi = 0.05$. For the side where bremsstrahlung losses are expected during the track extrapolation, the range in ϕ is increased to $\phi = 0.1$. If the track coincides with a track coming from a conversion vertex, than this candidate is treated as a photon[58].

Since unconverted photons do not have tracks in the inner tracker, they are reconstructed from clusters of energy deposits in the electromagnetic calorimeter that have no associated tracks in the inner detector.

In this analysis, photons are required to have $|\eta| < 2.37$ excluding the region $1.37 < |\eta| < 1.52$ and to have $p_{\text{T}} > 20\,\text{GeV}$. They are also required to pass the

tight ID criteria: They are also required to pass cuts optimised for real photon selection and discrimination from isolated photons from $\pi^0 \to \gamma\gamma$ on energy deposits in the strip layer and the middle layer of the electromagnetic calorimeter, the strip layer and the middle layer, shower shape and the fraction of energy deposited in the hadronic calorimeter. Tight ID for single photons from $h \to \gamma\gamma$ has an expected efficiency of ∼88 % to ∼90 % depending on the p_{T} of the photon [58].

5.2.3. Missing Transverse Energy

Missing energy is a measure of the p_{T} imbalance in the detector. It arises from detector inefficiencies, poor calibration, incorrect object reconstruction or identification, and the presence of invisible particles. It is the negative vector sum of the transverse momentum measured in the experiment. Missing energy is reconstructed by including contributions from fully reconstructed and calibrated particles and jets (hard objects) and from the soft event consisting of reconstructed charged particle tracks not associated with hard objects [59]. It is susceptible to pile-up which can add to the hard scatter signal and introduce signal remnants in the liquid argon calorimeter. The x- and y- components of the missing transverse energy are given by

$$E_{x(y)}^{\mathrm{miss}} = -\sum_{i \in \{\text{hard objects}\}} p_{x(y),i} \quad - \sum_{j \in \{\text{soft signals}\}} p_{x(y),j} \tag{5.2.1}$$

which leads to

$$\boldsymbol{E}_{\mathrm{T}}^{\mathbf{miss}} = \left(E_x^{\mathrm{miss}}, E_y^{\mathrm{miss}}\right) \tag{5.2.2}$$

for the missing transverse energy vector.

5.3. Event Selection

For a event to be considered in this analysis, it is required to have at least two photons, at least one τ_{had} candidate and at least one electron or muon, which are the candidates for a τ_{lep}. The respective particles with the highest p_{T} are chosen as the particles used in this analysis. There has to be a τ_{had} candidate

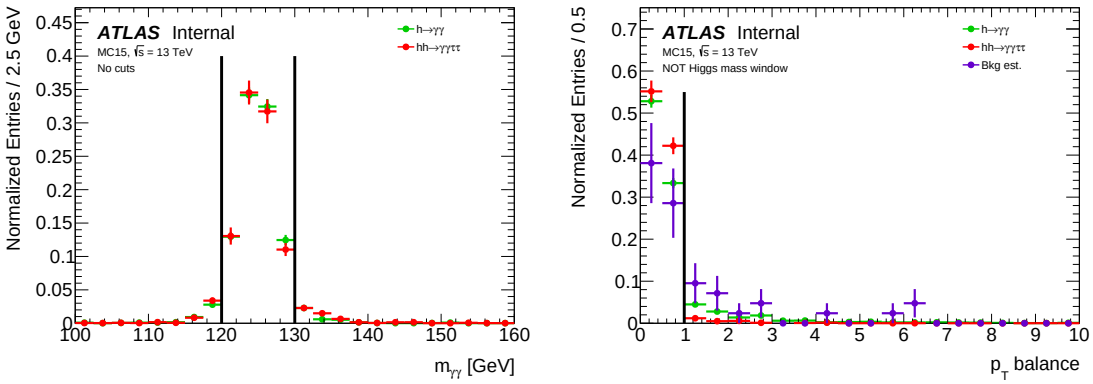

(a) $m_{\gamma\gamma}$, no cuts applied (b) p_{T}-balance, only $m_{\gamma\gamma}$ window cut applied

Figure 5.2.: Visualisation of the cut on $m_{\gamma\gamma}$ and the p_{T}-balance cut for the non-resonant di-Higgs production.

with $p_{\mathrm{T}} > 23\,\mathrm{GeV}$ and an electron or a muon with $p_{\mathrm{T}} > 15\,\mathrm{GeV}$. If this is not the case, a τ_{had} candidate with $p_{\mathrm{T}} > 20\,\mathrm{GeV}$ is also accepted, if the muon has $p_{\mathrm{T}} > 18\,\mathrm{GeV}$ or the electron has $p_{\mathrm{T}} > 22\,\mathrm{GeV}$.

Events are required to pass the high level trigger `HLT_2g20_tight`, which requires at least two tight photons with $p_{\mathrm{T}} > 20\,\mathrm{GeV}$. The τ_{had} candidate is required to fulfil the following additional quality criteria: It is required to have one or three prongs, $|\eta| < 2.5$ excluding $1.37 < |\eta| < 1.52$, $|Q| = 1$ and is required to pass the medium ID requirements. The τ_{lep} and the τ_{had} are required to have opposite-sign electrical charge. Moreover, a cut on the p_{T}-balance between the di-photon and di-τ-lepton system is implemented such that $p_{\mathrm{T,bal}} < 1$ as shown in fig. 5.2(b), where $p_{\mathrm{T,bal}}$ is defined as

$$p_{\mathrm{T,bal}} = \left| \frac{p_{\mathrm{T}}^{\gamma\gamma} - p_{\mathrm{T}}^{\tau\tau}}{p_{\mathrm{T}}^{\gamma\gamma}} \right|, \tag{5.3.1}$$

where p_{T}^{x} is the p_{T} of the four-vector sum of the visible parts of the particles x. The p_{T}-balance is expected to be small, since the Higgs bosons are expected to carry similar amounts of p_{T}. Furthermore, a cut on ΔR_{hh} with $\Delta R_{hh} > 1.8$ is applied for the resonant heavy Higgs analysis with $m_H = 260\,\mathrm{GeV}$ and a $\Delta R_{hh} > 2.72$ cut for all other m_H and the non resonant di-Higgs production. These cuts are shown in fig. 5.3. Additionally, a cut on the Higgs boson mass window from 120 GeV to 130 GeV in the $m_{\gamma\gamma}$ spectrum is applied as shown in fig. 5.2(a). How the cuts where chosen is explained in section 5.3.2.

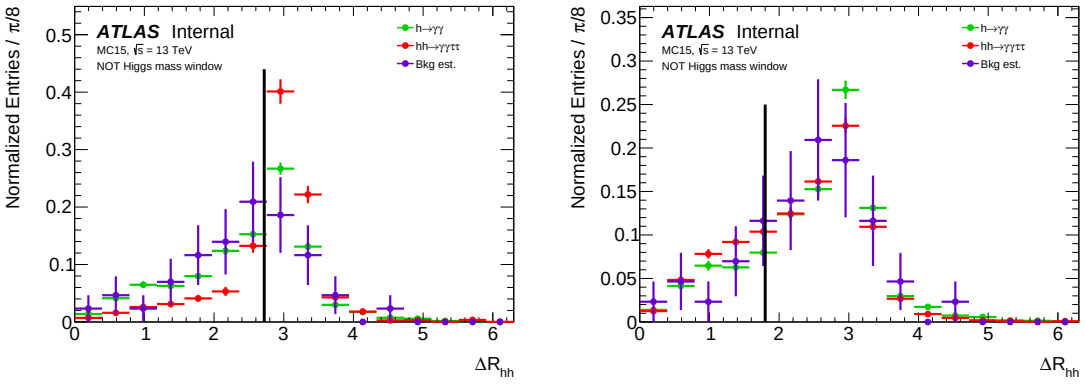

(a) non-resonant (b) $m_H = 260\,\text{GeV}$

Figure 5.3.: Visualisation of the cut on ΔR_{hh} for the non-resonant di-Higgs production as well as the resonant di-Higgs production for $m_H = 260\,\text{GeV}$ with only a cut on the Higgs mass window applied.

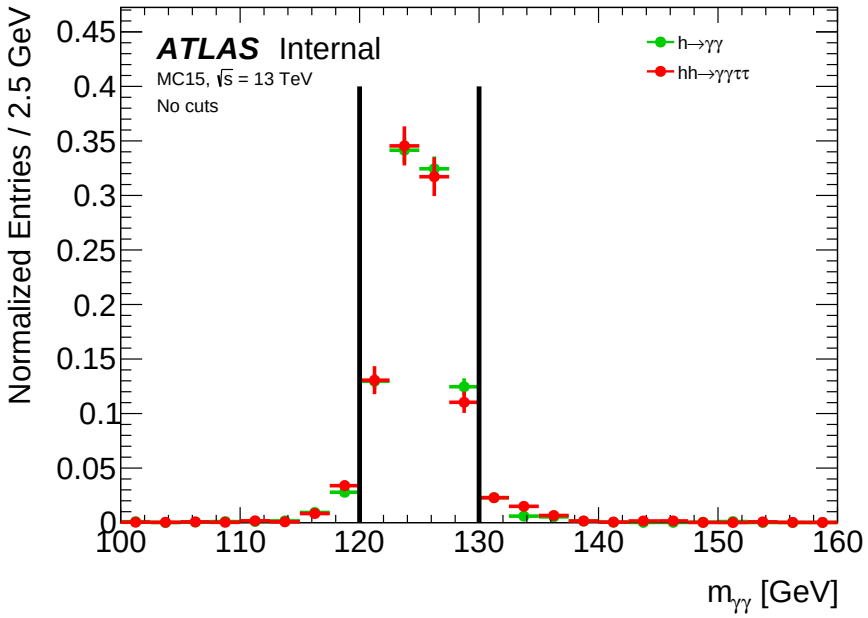

Figure 5.4.: Visualisation of the cut on $m_{\gamma\gamma}$ for the non-resonant di-Higgs production with no cuts applied.

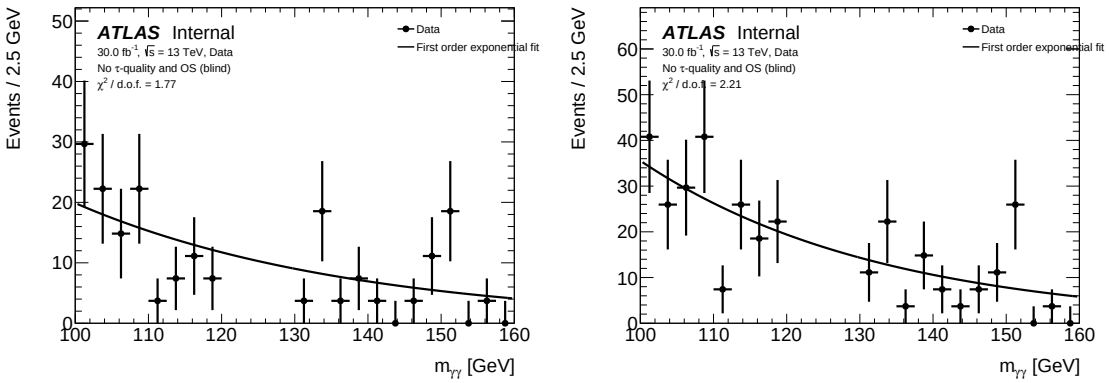

(a) Cuts for non-resonant and $m_H \neq 260\,\text{GeV}$ (b) Cuts for $m_H = 260\,\text{GeV}$

Figure 5.5.: First order exponential fit of the $m_{\gamma\gamma}$ spectrum to estimate the background in the $m_{\gamma\gamma}$ window from 120 GeV to 130 GeV. On the right the fit is shown for the cuts as applied for the $m_H = 260\,\text{GeV}$ resonant di-Higgs production and on the left the fit is shown for the cuts for all other heavy Higgs boson mass points and the non-resonant di-Higgs production.

5.3.1. Background Estimate

The only backgrounds estimated using MC samples are the SM $h \to \gamma\gamma$ processes as described in section 4.1. However, it is also necessary to estimate the underlying continuum background within the Higgs boson mass window. This is done using a fit in data in the side-bands, i. e., the regions, that are not within the Higgs boson mass window in the di-photon mass spectrum, and extrapolated into the Higgs boson mass window. Ideally, one would do the fit in the signal region (SR), i. e. with the final cuts applied. Due to statistical limitations this is not possible. Hence, the fits are done in the control region (CR), where only a preselection cut is applied: Compared to the final cuts, the τ_{had} candidates are not required to have medium ID and the τ-lepton candidates are not required to be of opposite sign in their electrical charge. The fit function used is a first order exponential function $f(x) = \exp(a + bx)$ is used. This is shown in fig. 5.5. The integral under the $f(x)$ in the Higgs mass window is then taken as the background estimate in the control region. To get the background estimate for the Higgs mass window in the signal region, this estimate is scaled by the ratio of the number of events in the side-bands in the CR and the SR:

$$n_{\text{bkg. est.}} = n_{\text{bkg. est. CR}} \frac{n_{\text{SR}}}{n_{\text{CR}}}, \tag{5.3.2}$$

with the ratio n_{SR}/n_{CR} being typically around 0.1. In the plots of distributions for different variables, this estimate of the continuum background is labelled as 'Bkg. est.'.

5.3.2. Event Selection Optimisation

The final event selection, as described above in section 5.3 was found by looking at different variables of the $\gamma\gamma$, $\tau_{\text{lep}}\tau_{\text{had}}$ and hh systems: ΔR_{hh}, $\Delta R_{\gamma\gamma}$, $\Delta R_{\tau_{\text{lep}}\tau_{\text{had}}}$, p_{T}-balance, $m_{\tau_{\text{lep}}\tau_{\text{had}}}$, $m_{\gamma\gamma}$ and $m_{\gamma\gamma\tau_{\text{lep}}\tau_{\text{had}}}$. Distributions for the variables cut on are shown in section 5.3 and appendix B. Distributions for the other variables are shown in fig. 5.6 for the non-resonant di-Higgs production and in appendix B for two different mass points for the resonant di-Higgs production. The mass of the $\tau_{\text{lep}}\tau_{\text{had}}$ system was reconstructed with three different methods: $m^{\text{vis}}_{\tau_{\text{lep}}\tau_{\text{had}}}$ is the mass of the detector visible components of the di-τ-lepton system. $m^{\text{coll}}_{\tau_{\text{lep}}\tau_{\text{had}}}$ is the mass given by the collinear approximation, where it is assumed, that the neutrinos in the decay are approximately collinear with the visible decay products and that the missing transverse energy is only from the neutrinos from the τ-lepton decays [60]. Hence, the mass reconstruction of the di-τ-lepton systems gets improved. $m^{\text{MMC}}_{\tau_{\text{lep}}\tau_{\text{had}}}$ is the mass given by the missing mass calculator as proposed in [61]. It improves even more on the mass reconstruction. The distributions for $\Delta R_{\gamma\gamma}$ and $\Delta R_{\tau_{\text{lep}}\tau_{\text{had}}}$ show that the for the non-resonant di-Higgs production and resonant di-Higgs production with high heavy Higgs boson masses, the di-photon and di-τ-lepton systems tend to be more boosted than for low heavy Higgs boson masses. This is due to the Higgs bosons having a smaller p_{T} for a low heavy Higgs boson mass.

In addition to the requirement, that the τ-lepton candidates have to be opposite sign, cutting only p_{T}-balance and the ΔR_{hh} turned out to be the most discriminating against background while not removing large amounts of signal.

The values for the p_{T}-balance and the ΔR_{hh} cuts were found by doing a two-dimensional optimisation on these values for an integrated luminosity of $30\,\text{fb}^{-1}$ for maximal significance. The significance used in this analysis is given as [62]

$$Z = \sqrt{2\left((s+b)\ln\frac{1+s}{b} - s\right)}, \tag{5.3.3}$$

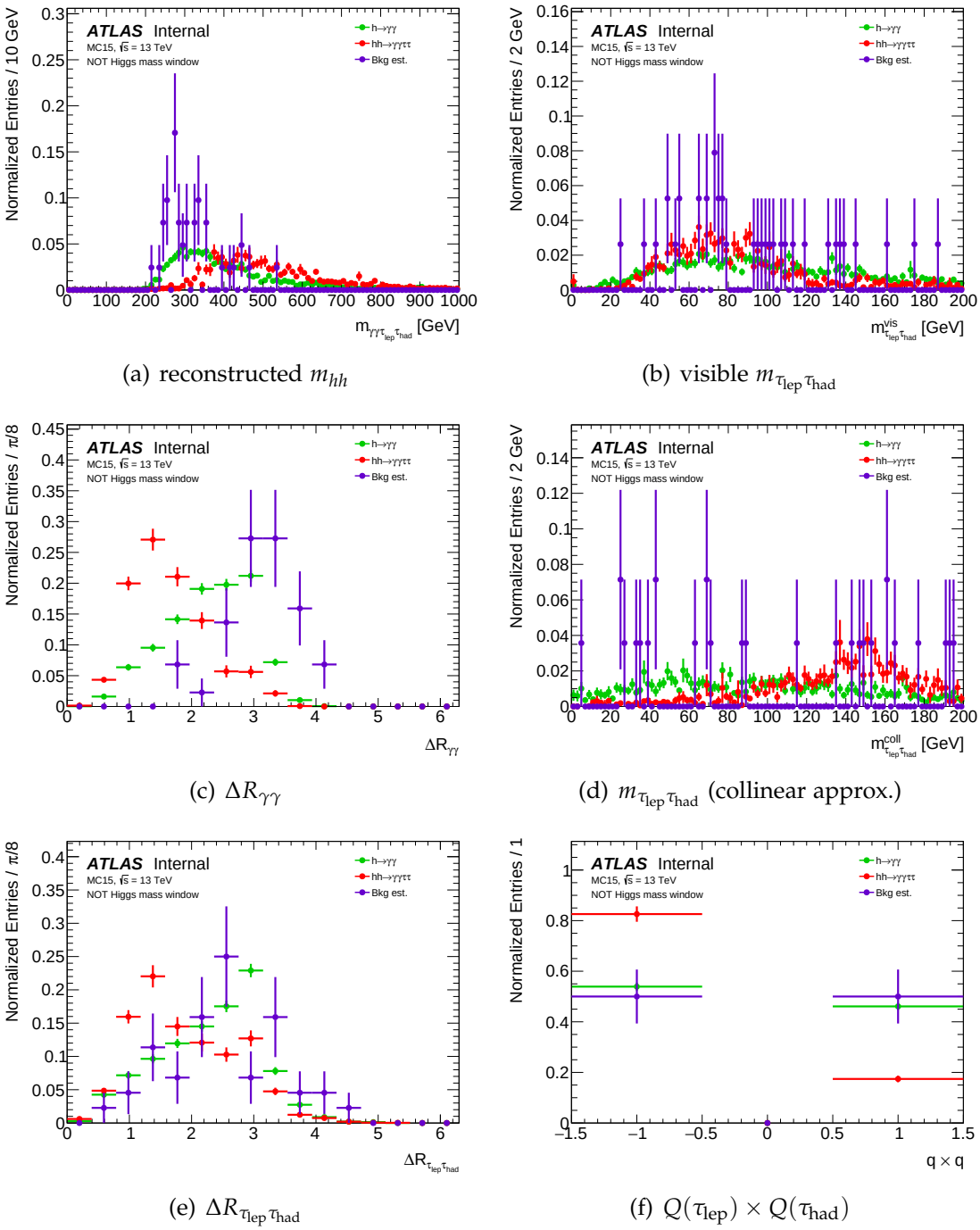

(a) reconstructed m_{hh}

(b) visible $m_{\tau_{\text{lep}}\tau_{\text{had}}}$

(c) $\Delta R_{\gamma\gamma}$

(d) $m_{\tau_{\text{lep}}\tau_{\text{had}}}$ (collinear approx.)

(e) $\Delta R_{\tau_{\text{lep}}\tau_{\text{had}}}$

(f) $Q(\tau_{\text{lep}}) \times Q(\tau_{\text{had}})$

Figure 5.6.: Distributions for different variables for the non-resonant di-Higgs production with only the cut on the $m_{\gamma\gamma}$ window applied.

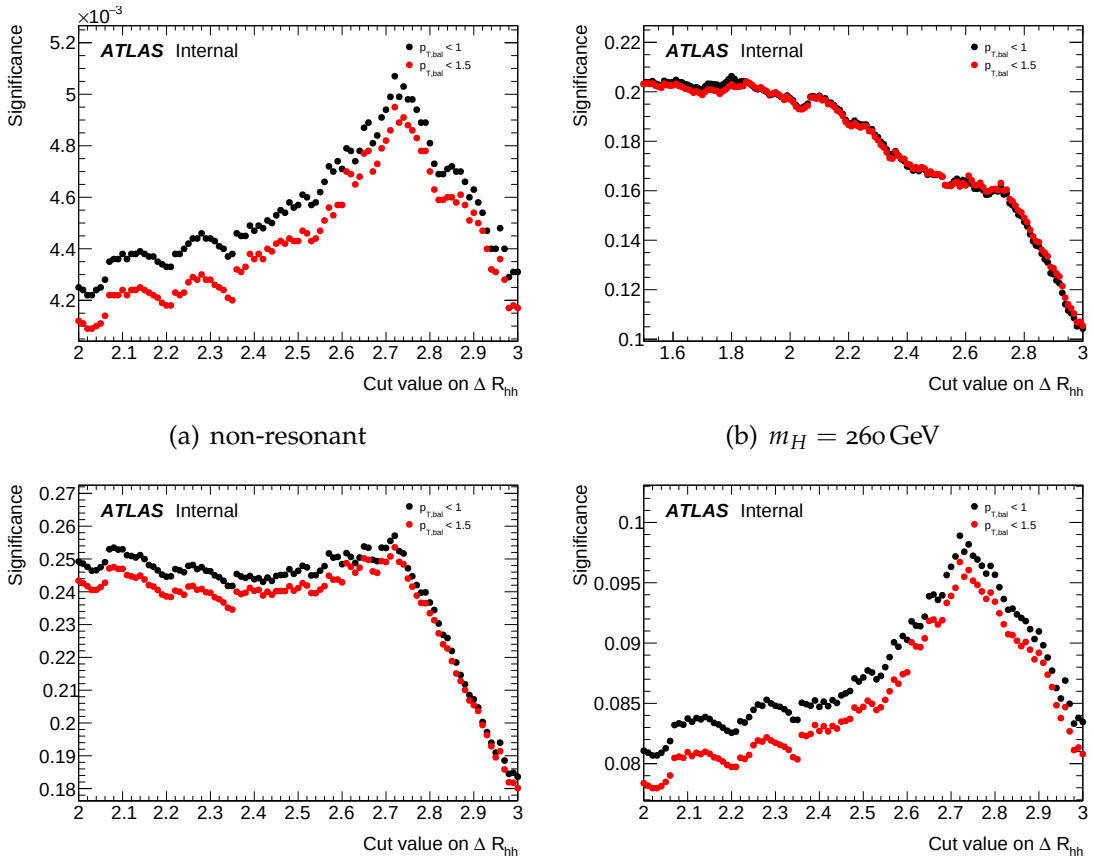

(a) non-resonant

(b) $m_H = 260\,\text{GeV}$

(c) $m_H = 300\,\text{GeV}$

(d) $m_H = 600\,\text{GeV}$

Figure 5.7.: Significance due to the chosen ΔR_{hh} cut for $p_{\text{T,bal}} < 1$ and $p_{\text{T,bal}} < 1.5$ for the non-resonant di-Higgs production and three different heavy Higgs boson masses. The cuts that give maximum significance are chosen as final cuts on ΔR_{hh} and the p_{T}-balance.

where s denotes the number of signal events and b the number of background events. This optimisation was done separately for the non-resonant case and for the different heavy Higgs boson masses and it was found that the same cut values were optimal for all mass points as well as the non-resonant sample. An example for the significance for different cuts on ΔR_{hh} and $p_{\text{T,bal}}$ for the non-resonant and resonant di-Higgs production for three different heavy Higgs masses is shown in fig. 5.7.

It is viable to do this optimisation of cuts on the p_{T}-balance and the ΔR_{hh}, since the background in the side-bands does not vary significantly for these variables as shown in fig. 5.8 and hence it can be assumed, that it behaves comparably int the m_h window.

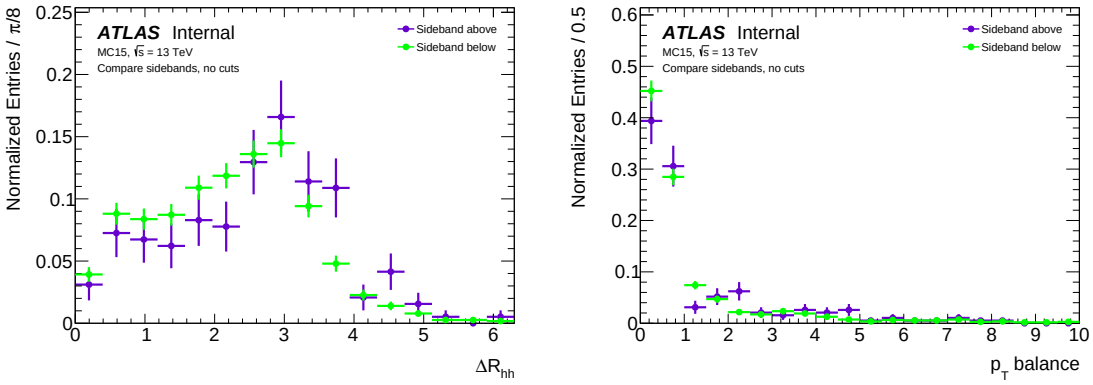

Figure 5.8.: Comparison of the ΔR_{hh} (left) and p_{T}-balance (right) of the events in the side-bands above and below the Higgs mass window. The spectra do not vary significantly.

5.3.3. Event Yields

In 2015 and 2016 8.1 fb^{-1} of data at a centre-of-mass energy $\sqrt{s} = 13\,\mathrm{TeV}$ were taken by ATLAS. Of this 8.1 fb^{-1} of data, 3.2 fb^{-1} were taken in 2015 and 4.9 fb^{-1} were taken in 2016. Until the end of 2016 it is expected that 30 fb^{-1} of data are taken by ATLAS. For the final selection of the signal, as described in section 5.3, cutflows for 8.1 fb^{-1} and 30 fb^{-1} for the non-resonant analysis, as well as the $m_H = 260\,\mathrm{GeV}$ and 600 GeV are listed in tables 5.1 to 5.4. The $h \to \gamma\gamma$ background is almost entirely removed and the continuum background is reduced by $\sim$97 %. For the non-resonant di-Higgs production and the high mass resonant di-Higgs production ($m_H = 600\,\mathrm{GeV}$) approximately one third of the events remain in the selection, while for the low mass di-Higgs production this is the case for only approximately one fourth of the events. This lower event yield for low m_H is due to them being, more often then not, not produced back-to-back as shown in fig. 5.9, which is the reason behind the different cut on ΔR_{hh}. Hence, for the low m_H the final cuts remove significantly more signal events than for heavy m_H of $m_H \geq 400\,\mathrm{GeV}$. All in all, the observed event yields are compatible with the background expectation as shown in tables 5.3 and 5.4.

For 8.1 fb^{-1} for the non-resonant di-Higgs production and the resonant di-Higgs production for all mass points except $m_H = 260\,\mathrm{GeV}$, the uncertainty on the background estimate and hence on the total background is larger than the event yield. This means, that there could be a negative amount of events, which is

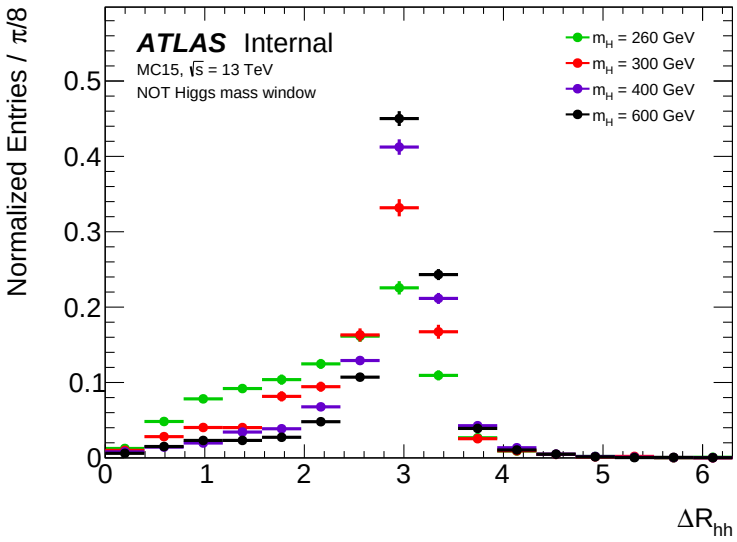

Figure 5.9.: ΔR_{hh} for different heavy Higgs masses. The higher the mass of the heavy Higgs, the more the two light Higgs boson tend to be back-to-back.

of course not possible. Hence, in future studies further studies will be needed, to get an background estimate with an uncertainity smaller than its nominal value.

Table 5.1.: Event yields for $30\,\text{fb}^{-1}$ and significance for the different cuts for the non-resonant di-Higgs production ($\sigma \times BR = 4.935\,\text{ab}$) as well as the resonant di-Higgs production for $m_H = 600\,\text{GeV}$ ($\sigma \times BR = 77.07\,\text{ab}$). Background estimate, the total background and the significance are only quoted when the background estimate is possible.

	Event yield			
	No cuts	Only Higgs mass window	Preselection cut	Final cut
$h \to \gamma\gamma$	2.62(5)	2.35(5)	0.98(3)	$7.4(8) \times 10^{-2}$
Continuum background		148(12)	39.8(63)	3.3(18)
Total background		151(12)	40(6)	3.4(18)
Non-resonant	$2.84(8) \times 10^{-2}$	$2.50(8) \times 10^{-2}$	$1.74(6) \times 10^{-2}$	$9.5(4) \times 10^{-3}$
Significance		2.03×10^{-3}	2.73×10^{-3}	5.16×10^{-3}
$m_H = 600\,\text{GeV}$	0.534(8)	0.471(7)	0.357(6)	0.187(4)
Significance		0.038	0.055	0.101

Table 5.2.: Event yields for $30\,\text{fb}^{-1}$ and significance for the different cuts for the resonant di-Higgs production for $m_H = 260\,\text{GeV}$ ($\sigma \times BR = 462.4\,\text{ab}$). Background estimate, the total background and the significance are only quoted when the background estimate is possible.

	Event yield			
	No cuts	Only Higgs mass window	Preselection cut	Final cut
$h \to \gamma\gamma$	2.62(5)	2.35(5)	1.57(4)	0.12(1)
Continuum background		148(12)	65.8(81)	6.2(25)
Total background		151(12)	67.4(81)	6.4(25)
$m_H = 260\,\text{GeV}$	1.83(3)	1.66(3)	0.93(2)	0.53(2)
Significance		0.135	0.113	0.208

Table 5.3.: Event yields for 8.1 fb^{-1} and significance for the different cuts for the non-resonant di-Higgs production ($\sigma \times BR = 4.935$ ab) as well as the resonant di-Higgs production for $m_H = 600$ GeV ($\sigma \times BR = 77.07$ ab). Background estimate, the total background and the significance are only quoted when the background estimate is possible.

	Event yield			
	No cuts	Only Higgs mass window	Preselection cut	Final cut
$h \to \gamma\gamma$	0.708(14)	0.633(13)	0.264(9)	0.020(2)
Continuum background		40.1(63)	10.7(33)	0.9(10)
Total background		40.8(63)	11.0(33)	0.9(10)
Non-resonant	$7.66(24) \times 10^{-3}$	$6.75(22) \times 10^{-3}$	$4.70(19) \times 10^{-3}$	$2.57(13) \times 10^{-3}$
Significance		1.06×10^{-3}	1.42×10^{-3}	2.68×10^{-3}
$m_H = 600$ GeV	0.144(2)	0.127(2)	$9.62(16) \times 10^{-2}$	$5.05(12) \times 10^{-2}$
Significance		0.02	0.029	0.052
Data	1385(38)	44(7)	13(4)	1(1)

Table 5.4.: Event yields for $8.1\,\mathrm{fb}^{-1}$ and significance for the different cuts for the resonant di-Higgs production for $m_H = 260\,\mathrm{GeV}$ ($\sigma \times BR = 462.4\,\mathrm{ab}$). Background estimate, the total background and the significance are only quoted when the background estimate is possible.

	Event yield			
	No cuts	Only Higgs mass window	Preselection cut	Final cut
$h \to \gamma\gamma$	0.708(14)	0.633(13)	0.425(11)	0.033(3)
Continuum background		40.1(63)	10.7(33)	1.7(13)
Total background		40.8(63)	18.2(42)	1.7(13)
$m_H = 260\,\mathrm{GeV}$	0.492(9)	0.447(9)	0.251(7)	0.144(5)
Significance		0.07	0.059	0.108
Data	1385(38)	44(7)	21(5)	2.0(14)

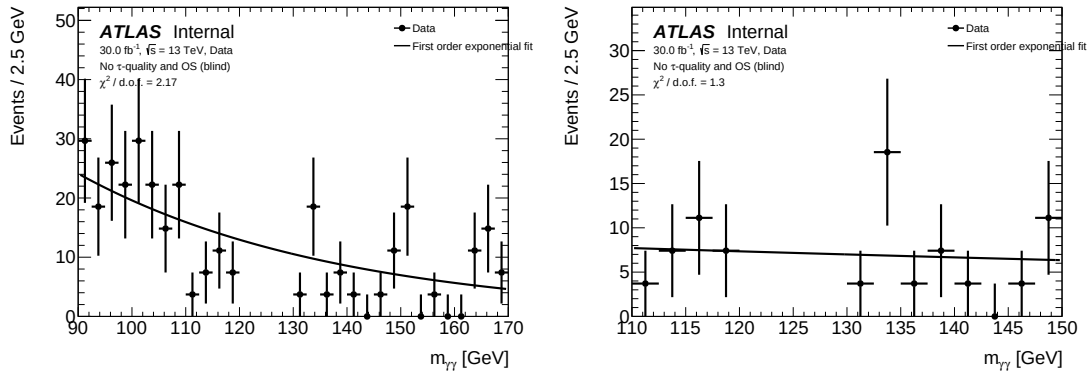

(a) Wide fit range

(b) Small fit range

Figure 5.10.: Variations on the fit range to estimate the systematic uncertainty due to it for cuts as applied for the non-resonant di-Higgs production. The left figure shows the fit for the $m_{\gamma\gamma}$ range from 90 GeV to 170 GeV, the right figure shows the fit fir the $m_{\gamma\gamma}$ range from 110 GeV to 150 GeV.

5.4. Systematic Uncertainties

Not only statistical uncertainties on the event yield but also systematic uncertainties have to be taken into account for the Monte Carlo samples and the data driven continuum background estimate to be able to describe the data reliably. The systematic uncertainties can change the nominal prediction and add an additional up- and downwards fluctuation on the event yield.

For the background estimate of the continuum background, as described in section 5.3.1, systematic uncertainties on the event yield due to the chosen fit range and due to uncertainties on the parameters of the fit are taken into account:

- The systematic uncertainty on the fit range was estimated by varying the side-bands: The fit was also done for ranges in $m_{\gamma\gamma}$ from 90 GeV to 170 GeV as largest range down to 110 GeV to 150 GeV as smallest range. 90 GeV to 170 GeV is chosen to be the largest fit range, since for fit ranges including events with $m_{\gamma\gamma} < 90$ GeV one would go beyond the Z-boson mass resonance and a simple exponential function would not be able to describe the data sufficiently. These upper and lower variations on the fit range are shown in fig. 5.10. For the preselection cuts as applied for the non-resonant di-Higgs production, this gives a factor of 31 % for the downwards and 14 % for the upwards variation of the event yield for the continuum background for cuts due to this uncertainty. Due to the different

cut on ΔR_{hh} for the $m_H = 260\,\text{GeV}$ di-Higgs production, there the variation factors on the event yield are 51 % (downwards) and 9 % (upwards).

- The systematic uncertainties on the parameters of the fit function amounts to $\pm 17\,\%$. Since the fit parameters are correlated, they are both scaled upwards and downwards respectively to get this uncertainty.

For the MC samples, systematic uncertainties on the event yield due to uncertainties on the reconstruction and the identification of the different objects and on the luminosity have been considered:

- The preliminary uncertainty on the combined 2015+2016 integrated luminosity is 2.9 %. It is derived, following a methodology similar to that detailed in [63], from a preliminary calibration of the luminosity scale using x-y beam-separation scans performed in August 2015 and May 2016.

- For electrons and photons the resolution of the detector, an overall correction scale factor and scale factors for the scintillator response, the electromagnetic calorimeter response and the temperature of the electromagnetic calorimeter are taken into account. Also, an additional scale factor for the electron and photon ID efficiencies, respectively, is taken into account.

- For muons, systematic uncertainties on the momentum scale, the reconstruction in the inner detector and the muon spectrometer and on the muon ID are taken into account.

- For τ_{had} candidates systematic uncertainties on the τ_{had} identification, the overlap removal with electrons, the reconstruction efficiency and the τ-lepton energy scale are taken into account.

- For missing transverse energy systematic uncertainties on the soft-track resolution and momentum scale are taken into account. Furthermore, systematic uncertainties on jets are taken into account. Since the calculation of missing transverse energy depends on the $p_{x(y)}$ of jets, in this analysis, these are effectively systematic uncertainties on the term for the hard objects of the missing transverse energy.

- The MC has been reweighted for the in 2015 data measured pile-up profile and an estimated pile-up profile for 2016. Uncertainties on these pile-up reweighting have been taken into account.

In addition to these, uncertainties on the cross-section times branching ratio were taken into account for the $h \to \gamma\gamma$ MC samples.

Values for $30\,\text{fb}^{-1}$ for the different systematic uncertainties considered for signal and background MC are shown in appendix C in detail, while the most significant systematic uncertainties are singled out in tables 5.5 to 5.8. They are at the highest in the order of 5 %, with the largest systematic uncertainty being on the photon identification efficiency.

Table 5.5.: Most significant systematics for the background MC for $30\,\text{fb}^{-1}$ for the cuts as applied for the non-resonant di-Higgs production.

Systematic	Variation on event yield [%] Downwards	Upwards
e/γ overall scale corr.	1.12	0.626
Luminosity	2.9	2.9
$E_{\text{T}}^{\text{miss}}$ soft term scale	−0.164	1.74
Photon ID eff.	4.59	4.7
τ_{had} ID total eff.	1.01	1.74
τ_{had} energy scale insitu	1.68	0.239
$\sigma \times$ BR	1.1	1.1

Table 5.6.: Most significant systematics for the non-resonant di-Higgs production MC for $30\,\text{fb}^{-1}$.

Systematic	Variation on event yield [%] Downwards	Upwards
e/γ overall scale corr.	0.287	−1.61
Luminosity	2.9	2.9
Photon ID eff.	4.43	4.53
τ_{had} ID total eff.	2.94	4.12
τ_{had} overlap rem. true τ_{had}	1.16	1.16
τ_{had} total reco. eff.	3.22	3.22
τ_{had} energy scale insitu	1.4	0.808

Table 5.7.: Most significant systematics for the resonant di-Higgs production MC for $m_H = 260\,\text{GeV}$ for $30\,\text{fb}^{-1}$.

Systematic	Variation on event yield [%] Downwards	Upwards
Luminosity	2.9	2.9
Photon ID eff.	4.45	4.55
τ_{had} ID total eff.	0.765	1.31
τ_{had} energy scale insitu	1.03	0.147

Table 5.8.: Most significant systematics for the resonant di-Higgs production MC for $m_H = 600\,\text{GeV}$ for $30\,\text{fb}^{-1}$.

Systematic	Variation on event yield [%] Downwards	Upwards
e/γ overall scale corr.	1.29	−0.893
Luminosity	2.9	2.9
Photon ID eff.	4.37	4.47
τ_{had} ID total eff.	3.01	5.21
τ_{had} overlap rem. true τ_{had}	1.2	1.2
τ_{had} total reco. eff.	3.03	3.03
τ_{had} energy scale insitu	1.75	1.06

6. Results

Based on the observed and predicted event yields in the signal region, for both non-resonant and resonant production, two results are presented here: The first set of results is obtained on 8.1 fb^{-1} of data taken by ATLAS in 2015 and 2016 at a centre-of-mass energy $\sqrt{s} = 13\,\text{TeV}$. These results are actual limits on $\sigma(gg \to hh) \times \text{BR}(hh \to \gamma\gamma\tau_{\text{lep}}\tau_{\text{had}})$.

The second set of results is obtained for 30 fb^{-1} of data. These results show which limits can be expected to be set with the full 2016 dataset.

All results were obtained by utilising HistFactory [64] and HistFitter [65] using the CLs method [66, 67].

6.1. Non-resonant di-Higgs Production

For the non-resonant di-Higgs production no excess was found in data. Hence, limits were set on $\sigma(gg \to hh) \times \text{BR}(hh \to \gamma\gamma\tau_{\text{lep}}\tau_{\text{had}})$. Observed and expected limits at 95 % confidence level for the signal hypothesis are shown in tables 6.1 and 6.2. With 30 fb^{-1} of data, the expected limit is one order of magnitude lower that the one that could be measured. Nevertheless, this is still three orders of magnitude higher than the SM expectation for the cross section times branching ratio of 4.395 ab. The cross section times branching ratio limits correspond to an observed (expected) limit of 10.3×10^3 (9.4×10^3) times the SM cross-section

Table 6.1.: Limits on $\sigma(gg \to hh) \times \text{BR}(hh \to \gamma\gamma\tau_{\text{lep}}\tau_{\text{had}})$ for 8.1 fb^{-1} with statistical uncertainty only and with the inclusion of systematic uncertainties.

	$\sigma \times BR$ limit at 95 % confidence level for the signal hypothesis [fb]	
	statistical unc. only	systematic unc. included
Expected	40^{-264}_{+13}	40^{-275}_{+13}
Observed	42	42

Table 6.2.: Expected limits on $\sigma(gg \to hh) \times \mathrm{BR}(hh \to \gamma\gamma\tau_{\mathrm{lep}}\tau_{\mathrm{had}})$ for 30 fb^{-1} with statistical uncertainty only and with the inclusion of systematic uncertainties.

$\sigma \times BR$ limit at 95 % confidence level for the signal hypothesis [fb]	
statistical unc. only	systematic unc. included
$5.9^{-13.5}_{+3.2}$	$5.9^{-13.4}_{+3.2}$

prediction for 8.1 fb^{-1} of data and 1.4×10^3 (1.4×10^3) times the SM cross-section prediction for 30 fb^{-1} of data. The inclusion of systematic uncertainties has an impact of less than 1 % on the measured values.

6.2. Resonant di-Higgs Production

For the resonant di-Higgs production no excess was found in data. Hence, limits were set on $\sigma(gg \to H) \times \mathrm{BR}(hh \to \gamma\gamma\tau_{\mathrm{lep}}\tau_{\mathrm{had}})$ in the same manner as it was done for the non-resonant di-Higgs production. For only considering statistical errors, these limits are shown in figs. 6.1 and 6.2. Limits that take systematic uncertainties into account are shown in figs. 6.3 and 6.4. As for the non-resonant case, going from 8.1 fb^{-1} to 30 fb^{-1} of data increases the expected limit about one order of magnitude. The inclusion of systematic uncertainty also has an impact of less than 1 % on the measured values.

Table 6.3.: Limits on $\sigma(gg \to H) \times \mathrm{BR}(hh \to \gamma\gamma\tau_{\mathrm{lep}}\tau_{\mathrm{had}})$ for 8.1 fb^{-1} with statistical uncertainty only and with the inclusion of systematic uncertainties.

m_H [GeV]		$\sigma \times BR$ limit at 95 % confidence level for the signal hypothesis [fb]	
		statistical unc. only	systematic unc. included
260	Expected	38^{+71}_{-20}	38^{+72}_{-20}
	Observed	43	43
600	Expected	30^{+141}_{-20}	30^{+141}_{-20}
	Observed	31	31

Table 6.4.: Expected limits on $\sigma(gg \to H) \times \mathrm{BR}(hh \to \gamma\gamma\tau_{\mathrm{lep}}\tau_{\mathrm{had}})$ for $30\,\mathrm{fb}^{-1}$ with statistical uncertainty only and with the inclusion of systematic uncertainties.

	$\sigma \times BR$ limit at 95 % confidence level for the signal hypothesis [fb]	
m_H [GeV]	statistical unc. only	systematic unc. included
260	$10.3^{+9.0}_{-4.0}$	$10.6^{+8.9}_{-4.0}$
600	$4.8^{+5.5}_{-1.9}$	$4.8^{+5.8}_{-2.1}$

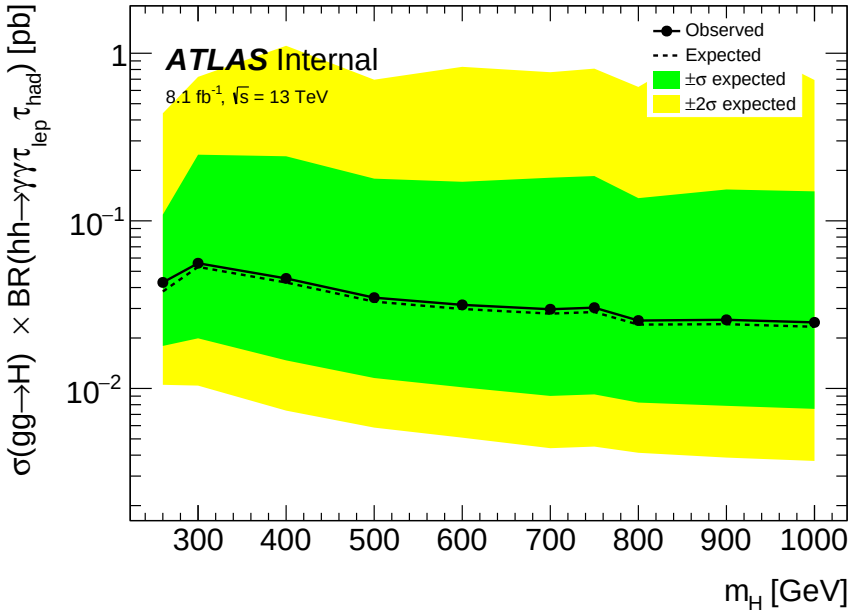

Figure 6.1.: Limits on $\sigma(gg \to H) \times \mathrm{BR}(hh \to \gamma\gamma\tau_{\mathrm{lep}}\tau_{\mathrm{had}})$ for $8.1\,\mathrm{fb}^{-1}$ for statistical errors only.

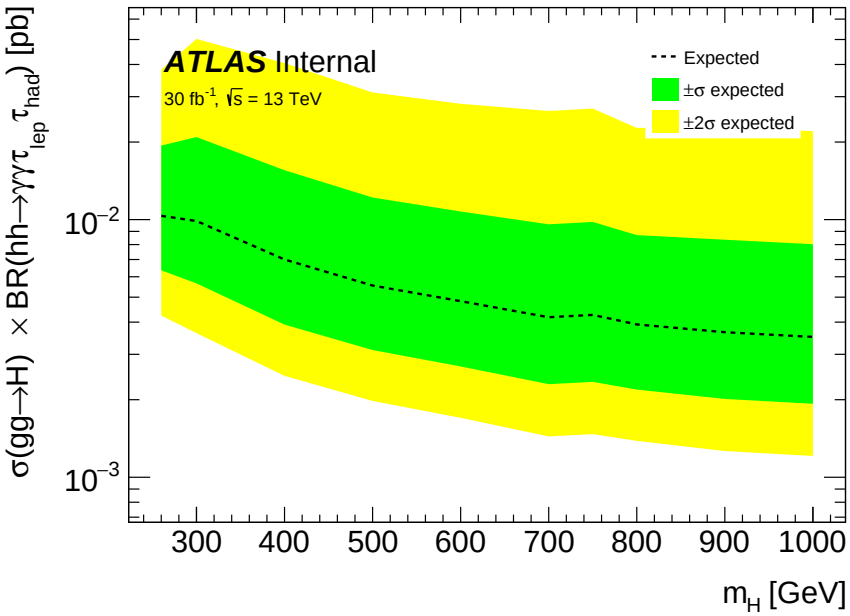

Figure 6.2.: Limits on $\sigma(gg \to H) \times \mathrm{BR}(hh \to \gamma\gamma\tau_{\mathrm{lep}}\tau_{\mathrm{had}})$ for $30\,\mathrm{fb}^{-1}$ for statistical errors only. The observed limit is given for the case, that the number of measured events is identical to the background events.

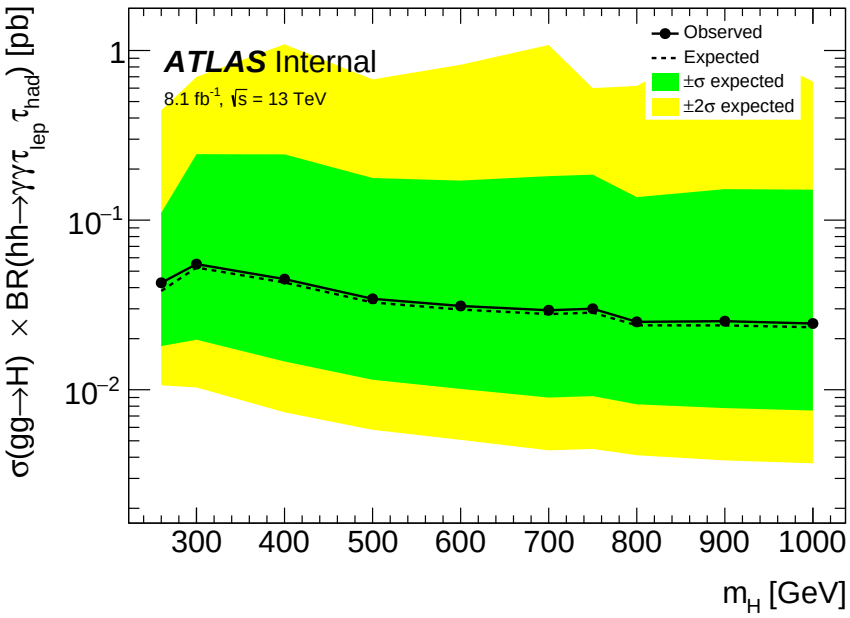

Figure 6.3.: Limits on $\sigma(gg \to H) \times \mathrm{BR}(hh \to \gamma\gamma\tau_{\mathrm{lep}}\tau_{\mathrm{had}})$ for $8.1\,\mathrm{fb}^{-1}$ with systematic errors included.

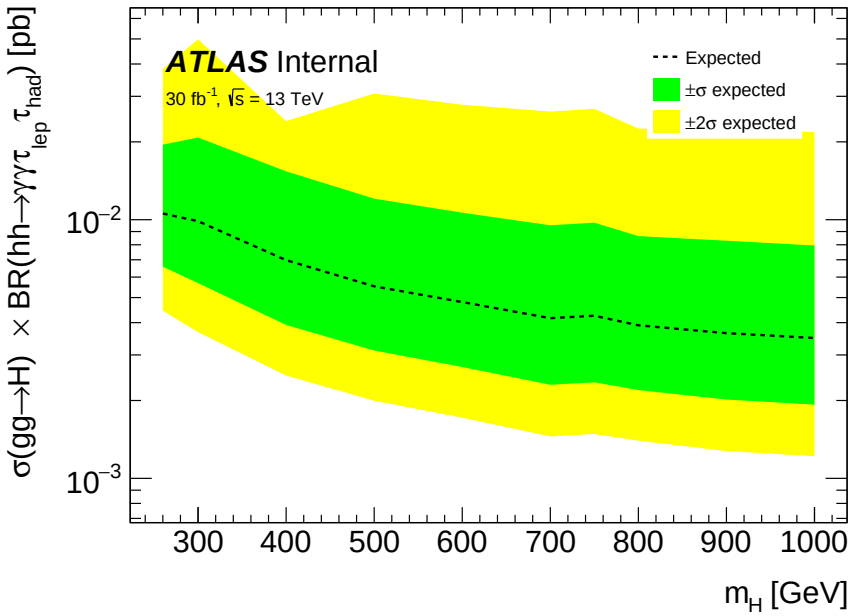

Figure 6.4.: Limits on $\sigma(gg \to H) \times \mathrm{BR}(hh \to \gamma\gamma\tau_{\mathrm{lep}}\tau_{\mathrm{had}})$ for $30\,\mathrm{fb}^{-1}$ with systematic errors included. The observed limit is given for the case, that the number of measured events is identical to the background events.

7. Conclusion and Outlook

In the course of this thesis a next-to-leading order effective field theory MC model for 2HDM was made available in the ATLAS software framework. Current and future analyses will benefit from its improved predictions in comparison to the Born-level MC that was available beforehand.

Furthermore, limits on the cross-section times branching ratio are set for the $hh \to \gamma\gamma\tau_{\text{lep}}\tau_{\text{had}}$-channel for resonant and non-resonant di-Higgs production, with data statistics being the limiting factor. When taking into account the increase of the different cross-sections for the di-Higgs production at $\sqrt{s} = 13\,\text{TeV}$ compared to the ones at $\sqrt{s} = 8\,\text{TeV}$ the limits on the resonant production are approximately the same order of magnitude as the ones set on $\sigma(gg \to H) \times \text{BR}(H \to hh)$ by ATLAS [24].

Nevertheless, the results show, that, in the coming years, it would make sense to investigate the $hh \to \gamma\gamma\tau_{\text{lep}}\tau_{\text{had}}$-channel, since it can potentially contribute to a combined measurement with several channels for di-Higgs production, especially as more data become available. With more data, better cuts or more sophisticated methods, such as boosted decision trees, could be implemented, since statistical limitations would be significantly less and lead to better limits.

The measurement of the non-resonant di-Higgs production and hence, the measurement of the Higgs boson self-coupling are within the reach of the LHC, a precision of $\sim$40 % could be reached with the $3\,\text{ab}^{-1}$ of data expected until 2030. In this data, $\mathcal{O}(10^5)$ SM di-Higgs boson events are expected with 30 to 40 events having a $\gamma\gamma\tau\tau$ final state. New physics beyond the SM can increase the number of di-Higgs boson events and will be needed to see an excess in the $\gamma\gamma\tau\tau$ final state in the near future.

A. Resonant Signal MC Validation

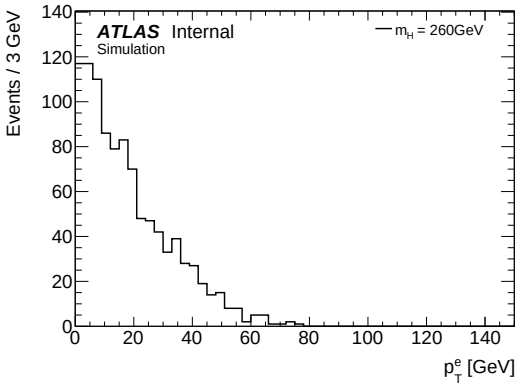

(a) $m_H = 260\,\text{GeV}$

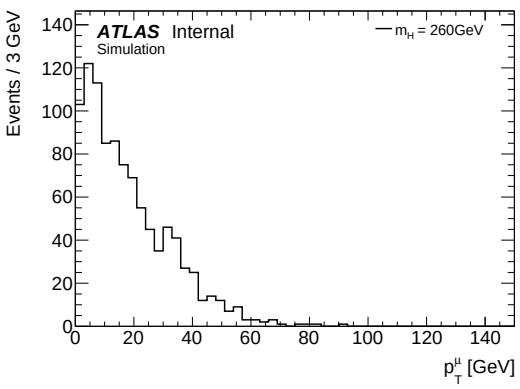

(b) $m_H = 260\,\text{GeV}$

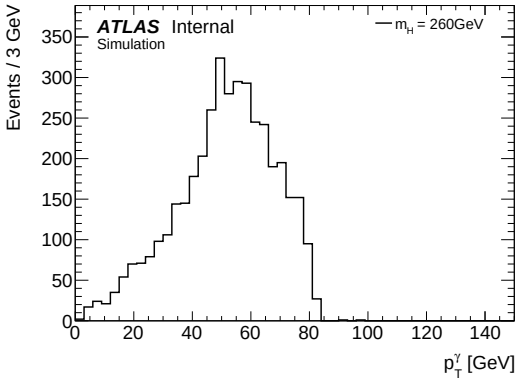

(c) $m_H = 260\,\text{GeV}$

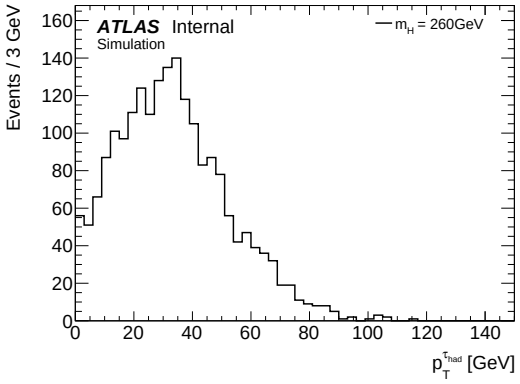

(d) $m_H = 260\,\text{GeV}$

Figure A.1.: Final state particle p_T-distributions on generator truth level for the resonant production for $m_H = 260\,\text{GeV}$ for a validation sample containing 2000 events.

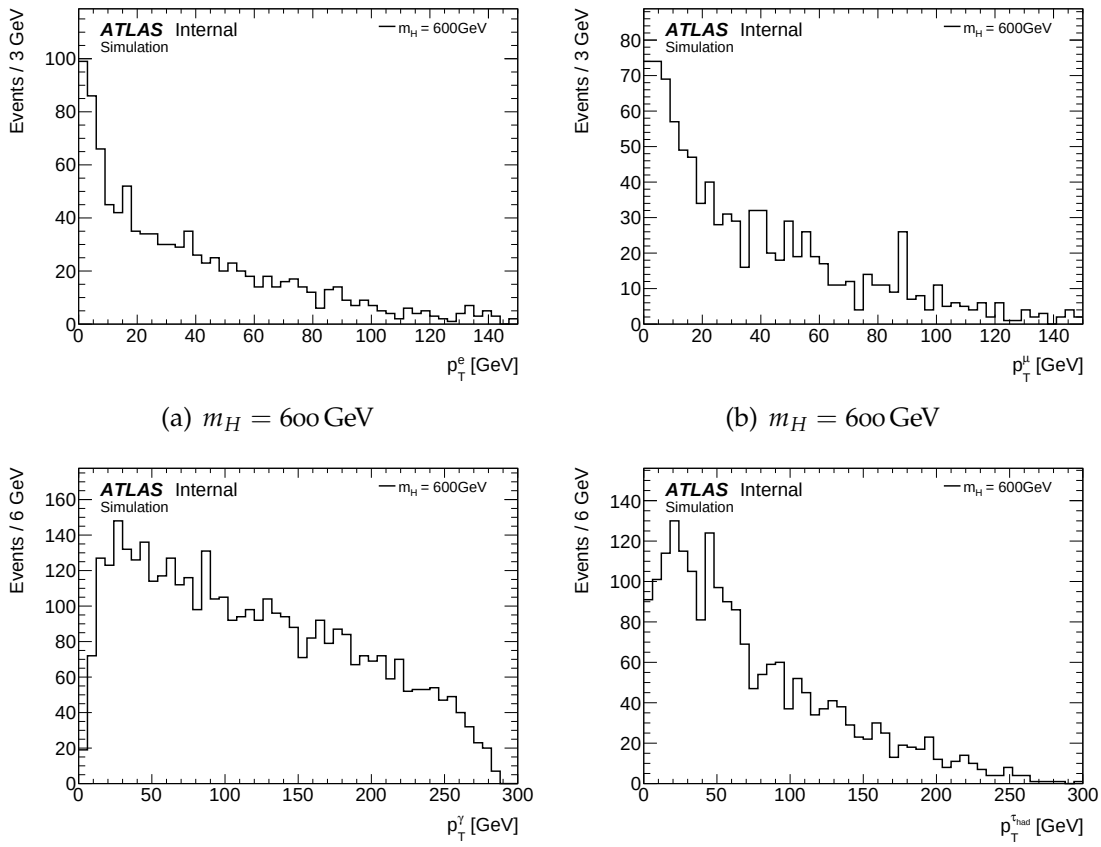

(a) $m_H = 600\,\text{GeV}$ (b) $m_H = 600\,\text{GeV}$

(c) $m_H = 600\,\text{GeV}$ (d) $m_H = 600\,\text{GeV}$

Figure A.2.: Final state particle p_T-distributions on generator truth level for the resonant production for $m_H = 600\,\text{GeV}$ for a validation sample containing 2000 events.

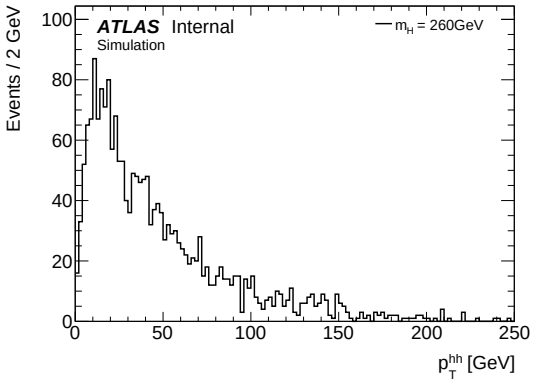

(a) $m_H = 260\,\text{GeV}$

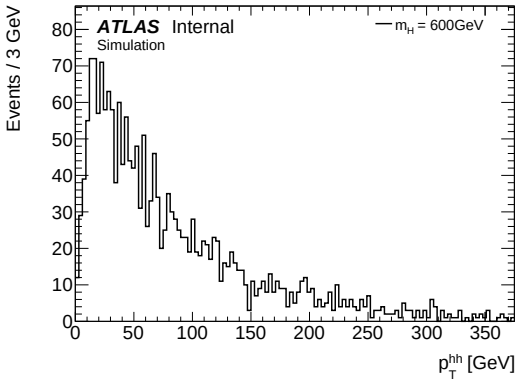

(b) $m_H = 600\,\text{GeV}$

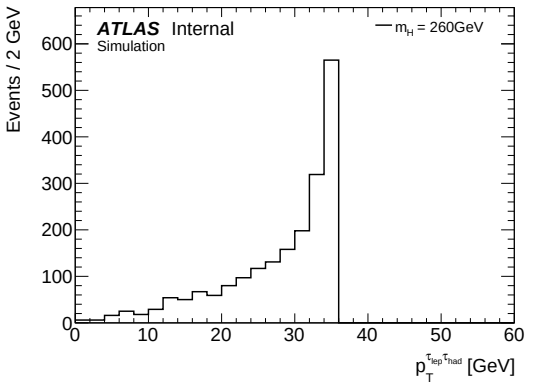

(c) $m_H = 260\,\text{GeV}$

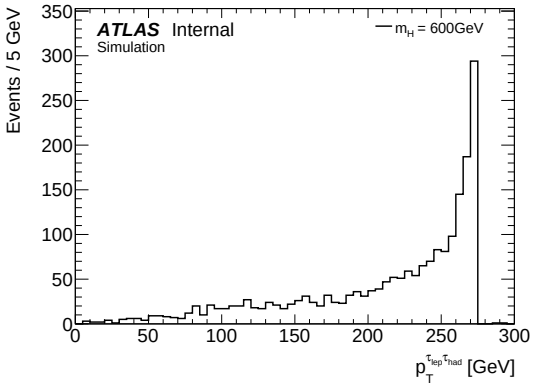

(d) $m_H = 600\,\text{GeV}$

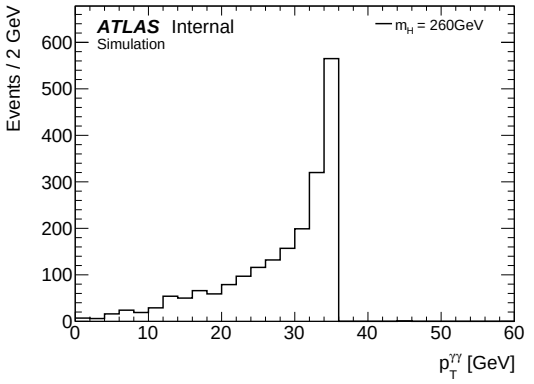

(e) $m_H = 260\,\text{GeV}$

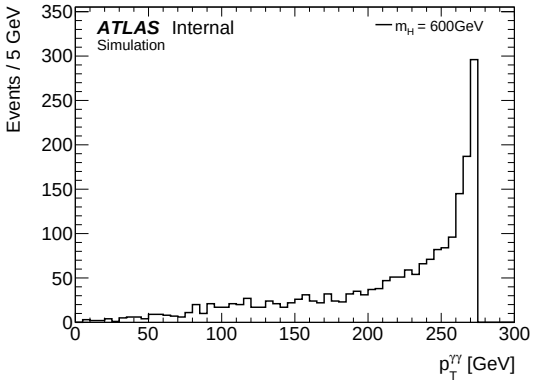

(f) $m_H = 600\,\text{GeV}$

Figure A.3.: Di-particle p_{T}-distributions on generator truth level for the resonant production for $m_H = 260\,\text{GeV}$ and $m_H = 600\,\text{GeV}$ for validation samples containing 2000 events.

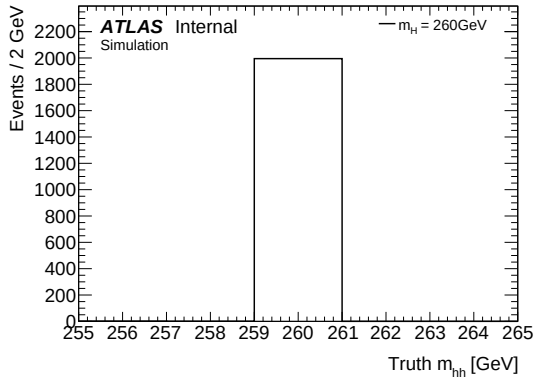

(a) $m_H = 260\,\text{GeV}$

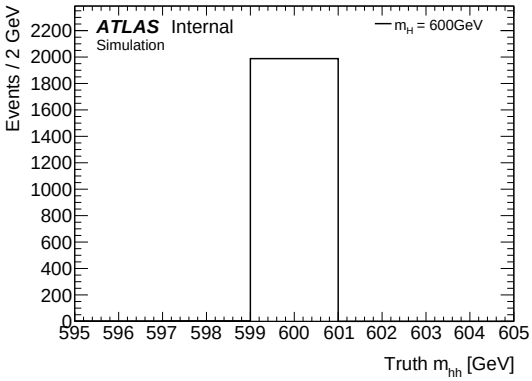

(b) $m_H = 600\,\text{GeV}$

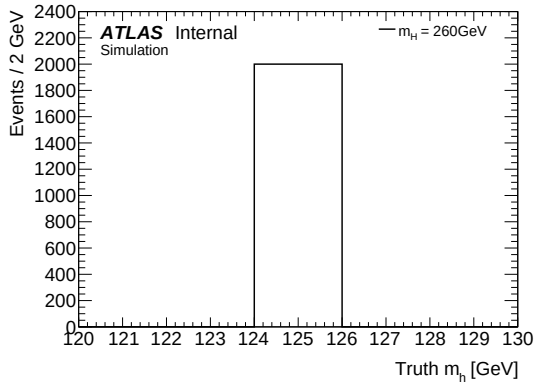

(c) $m_H = 260\,\text{GeV}$

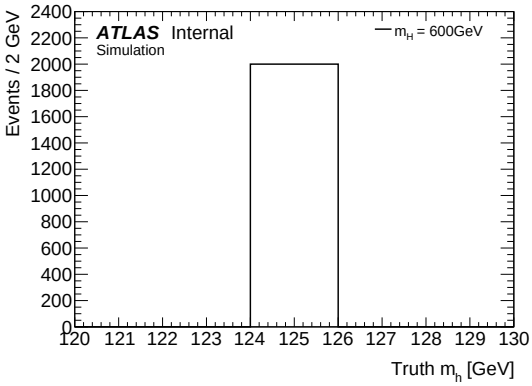

(d) $m_H = 600\,\text{GeV}$

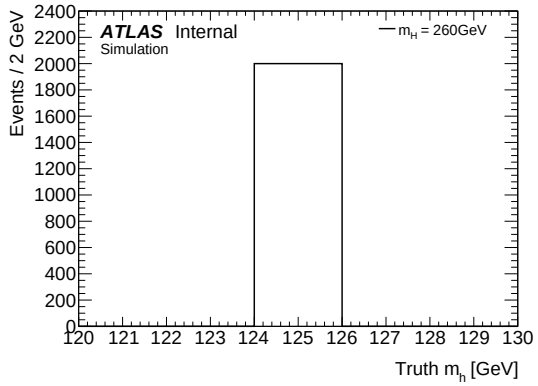

(e) $m_H = 260\,\text{GeV}$

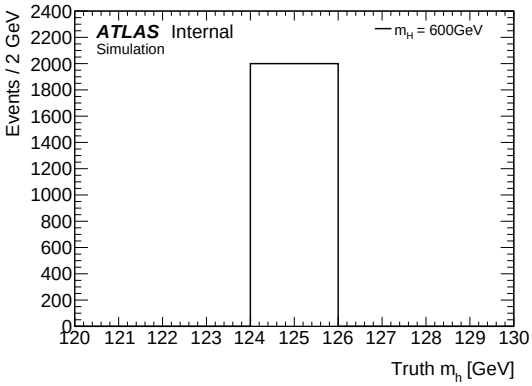

(f) $m_H = 600\,\text{GeV}$

Figure A.4.: Di-particle mass distributions on generator truth level for the resonant production for $m_H = 260\,\text{GeV}$ and $m_H = 600\,\text{GeV}$ for validation samples containing 2000 events.

B. Investigated Variables

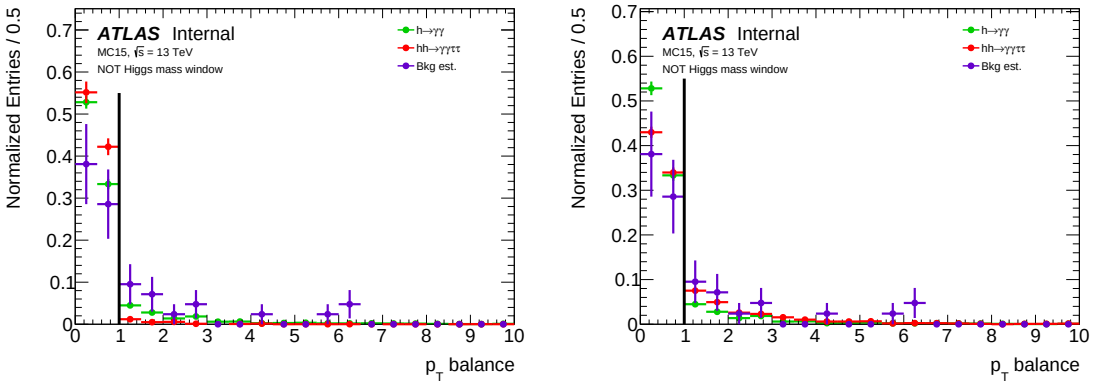

(a) non-resonant

(b) $m_H = 260\,\text{GeV}$

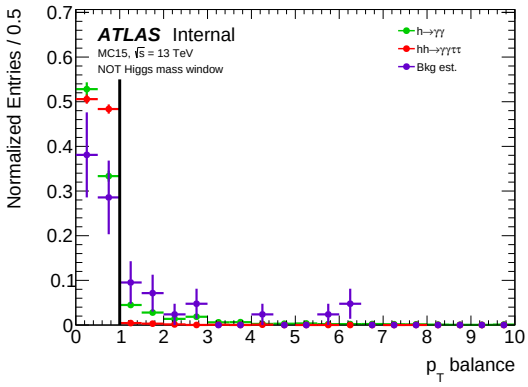

(c) $m_H = 600\,\text{GeV}$

Figure B.1.: Visualisation of the p_T-balance cut for the non-resonant di-Higgs production as well as the resonant di-Higgs production for $m_H = 260\,\text{GeV}$ and $m_H = 600\,\text{GeV}$ with only a cut on the Higgs mass window applied.

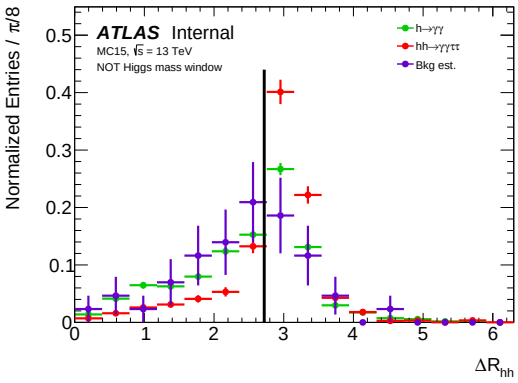

(a) non-resonant

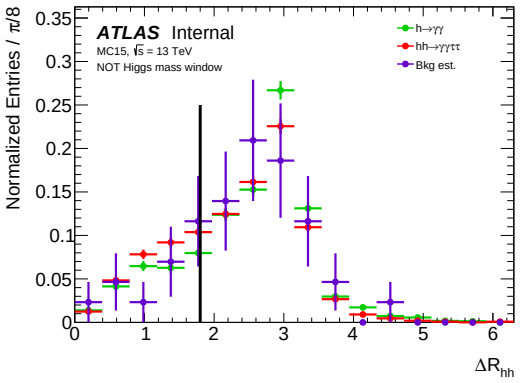

(b) $m_H = 260\,\text{GeV}$

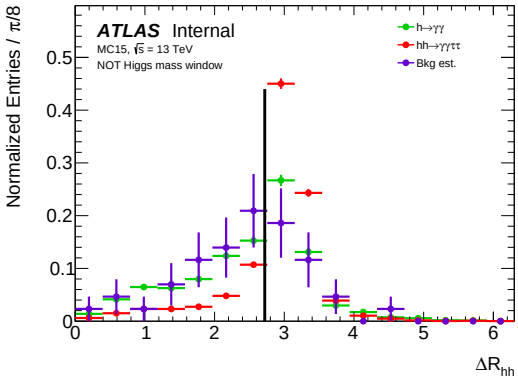

(c) $m_H = 600\,\text{GeV}$

Figure B.2.: Visualisation of the cut on ΔR_{hh} for the non-resonant di-Higgs production as well as the resonant di-Higgs production for $m_H = 260\,\text{GeV}$ and $m_H = 600\,\text{GeV}$ with only a cut on the Higgs mass window applied.

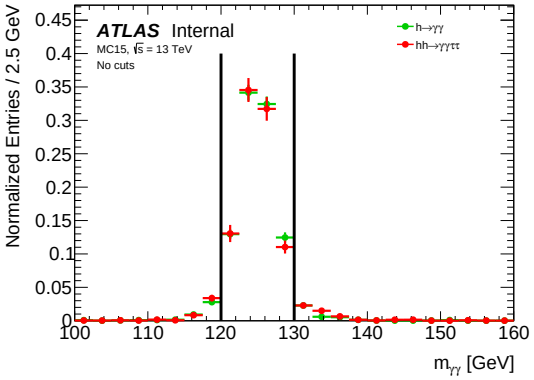

(a) non-resonant

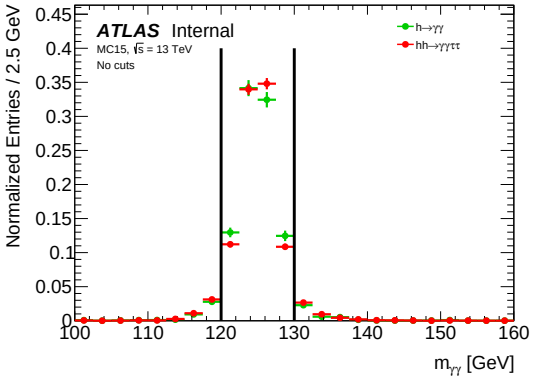

(b) $m_H = 600\,\text{GeV}$

Figure B.3.: Visualisation of the cut on $m_{\gamma\gamma}$ for the non-resonant and resonant di-Higgs production for $m_H = 600\,\text{GeV}$ with no cuts applied.

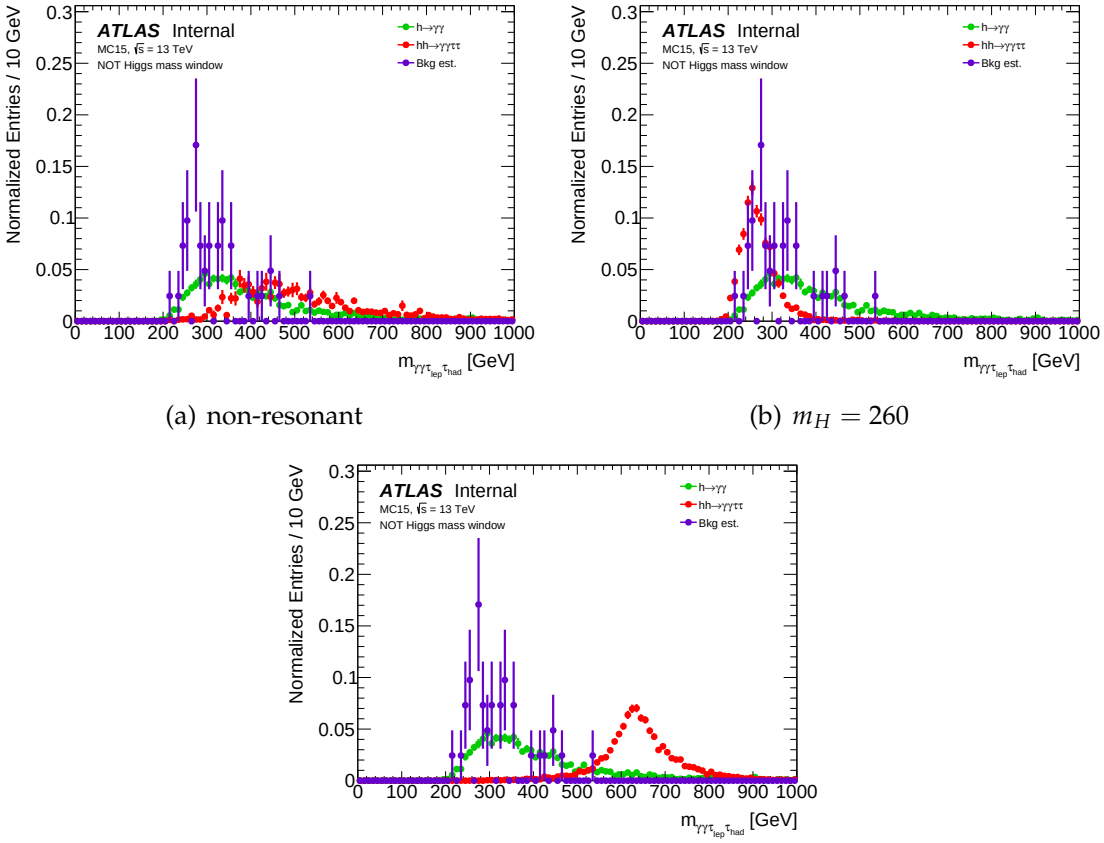

(a) non-resonant

(b) $m_H = 260$

(c) $m_H = 600$

Figure B.4.: Mass of the $\gamma\gamma\tau_{\text{lep}}\tau_{\text{had}}$ system with only the cut on the $m_{\gamma\gamma}$ window applied. Peaks for the respective heavy Higgs masses are clearly visible.

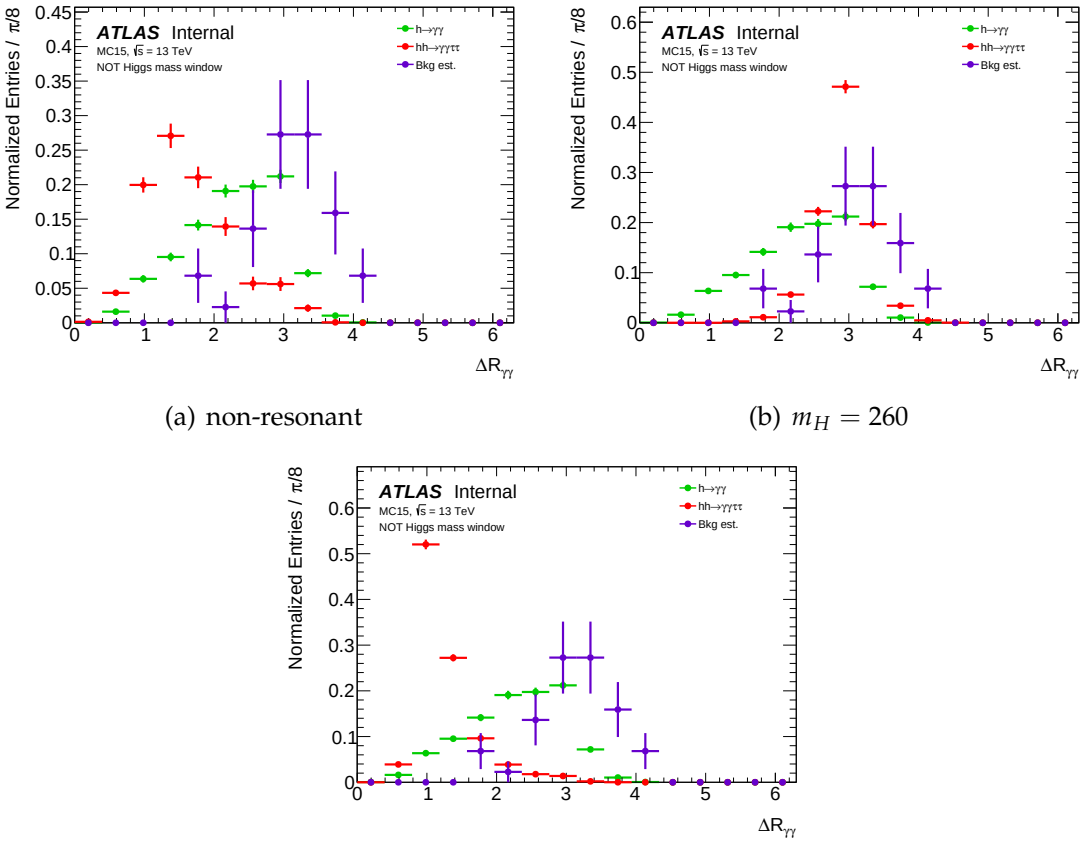

(a) non-resonant

(b) $m_H = 260$

(c) $m_H = 600$

Figure B.5.: ΔR between the two photons with only the cut on the $m_{\gamma\gamma}$ window applied. For the non-resonant di-Higgs production and resonant di-Higgs production with large mass heavy Higgs boson, the photons tend to be closer to each other. For light heavy Higgs boson, they tend to be more back-to-back.

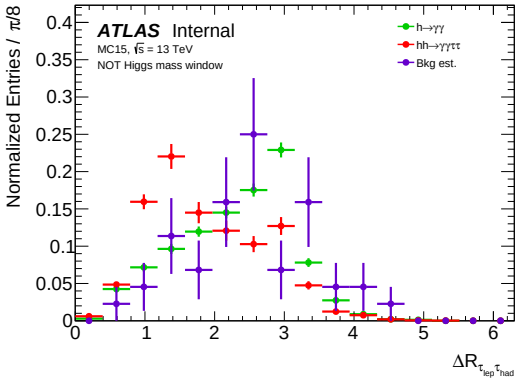

(a) non-resonant

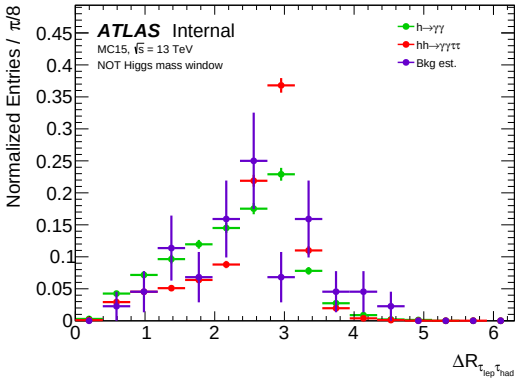

(b) $m_H = 260$

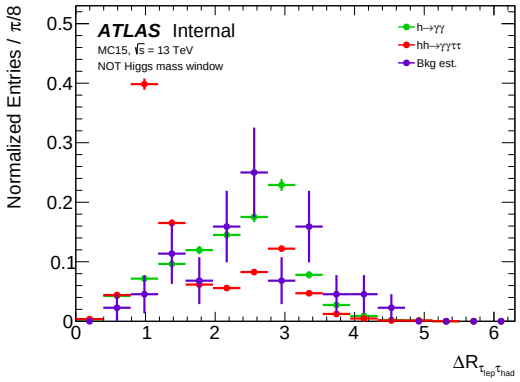

(c) $m_H = 600$

Figure B.6.: ΔR between τ_{lep} and τ_{had} with only the cut on the $m_{\gamma\gamma}$ window applied. For the non-resonant di-Higgs production and resonant di-Higgs production with large mass heavy Higgs boson, the photons tend to be closer to each other. For light heavy Higgs boson, they tend to be more back-to-back.

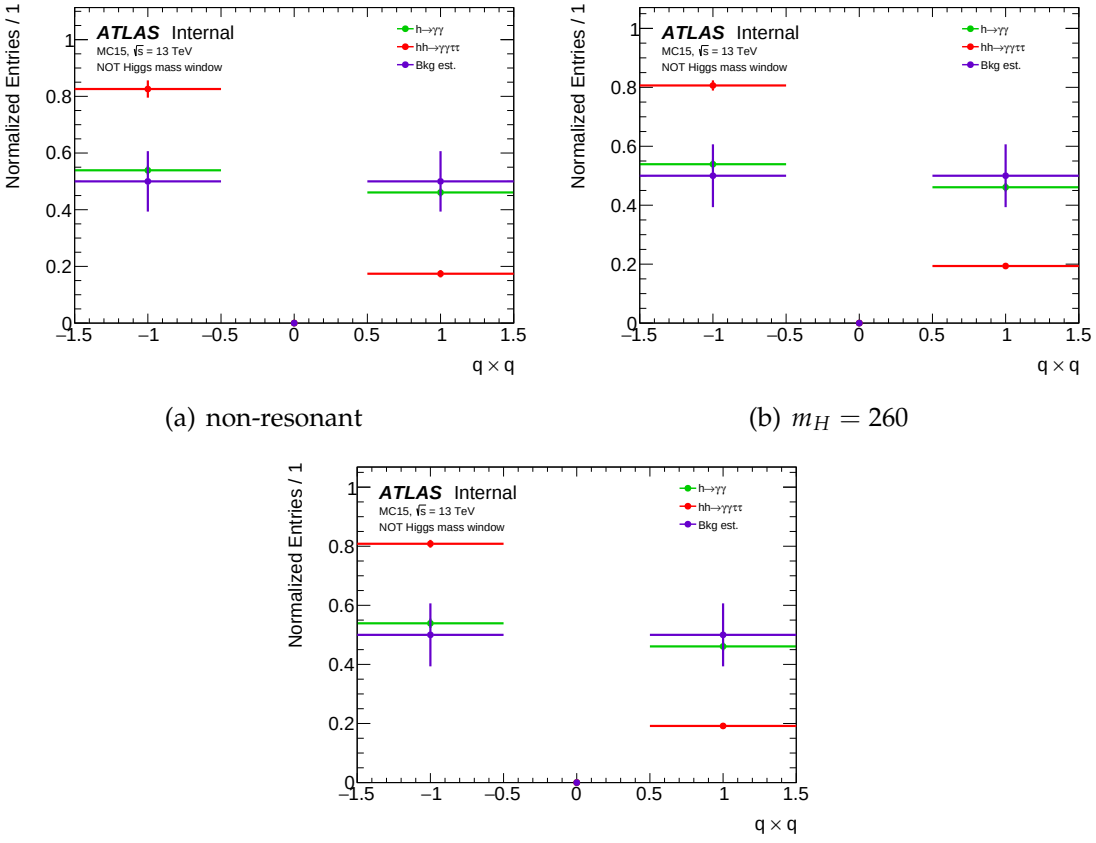

(a) non-resonant

(b) $m_H = 260$

(c) $m_H = 600$

Figure B.7.: $Q(\tau_{\text{lep}}) \times Q(\tau_{\text{had}})$ with only the cut on the $m_{\gamma\gamma}$ window applied. For the signal MC, the contribution at $Q(\tau_{\text{lep}}) \times Q(\tau_{\text{had}}) = 1$ is due to misidentification of the charge of either the τ_{lep} or the τ_{had}

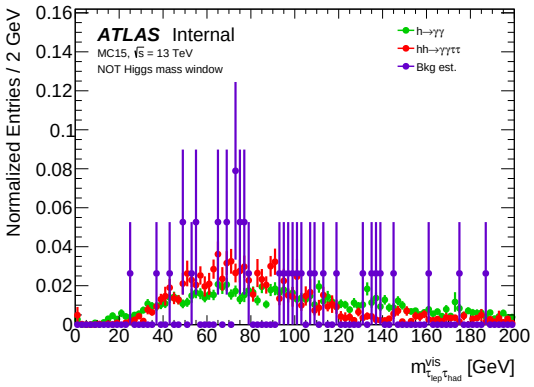

(a) non-resonant

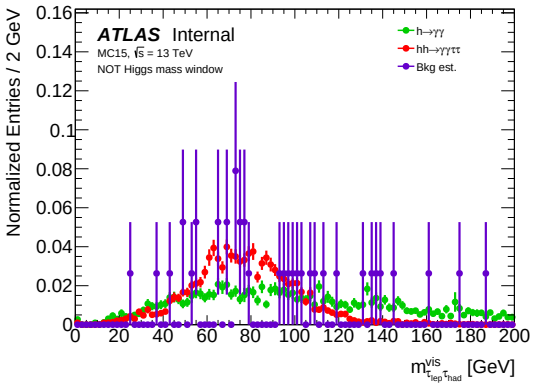

(b) $m_H = 260$

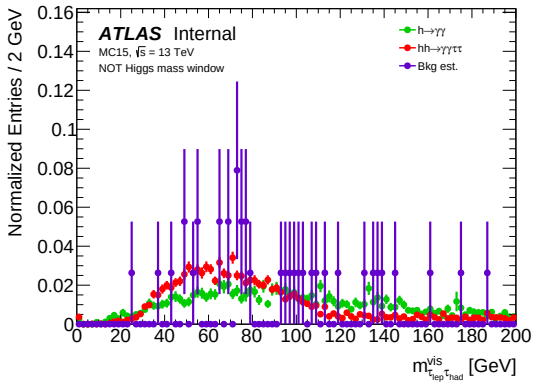

(c) $m_H = 600$

Figure B.8.: $m^{\text{vis}}_{\tau_{\text{lep}}\tau_{\text{had}}}$ with only the cut on the $m_{\gamma\gamma}$ window applied.

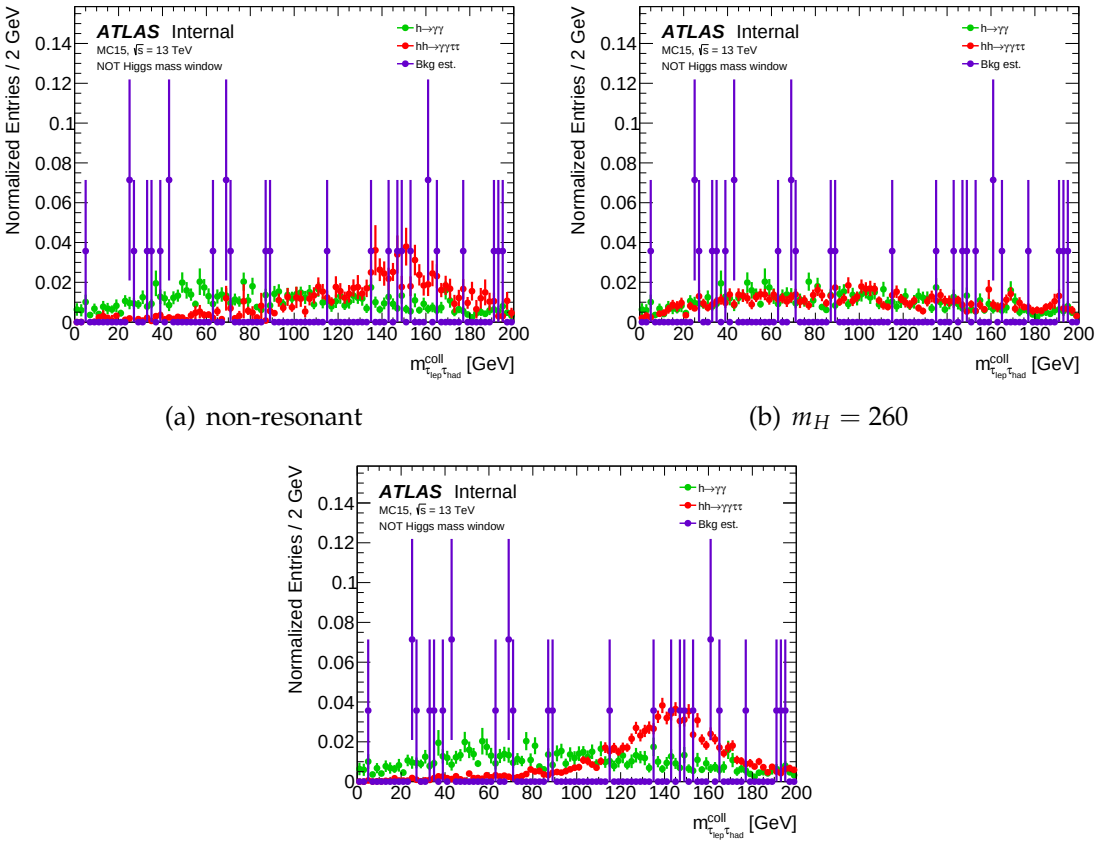

(a) non-resonant

(b) $m_H = 260$

(c) $m_H = 600$

Figure B.9.: $m^{\text{coll}}_{\tau_{\text{lep}}\tau_{\text{had}}}$ with only the cut on the $m_{\gamma\gamma}$ window applied.

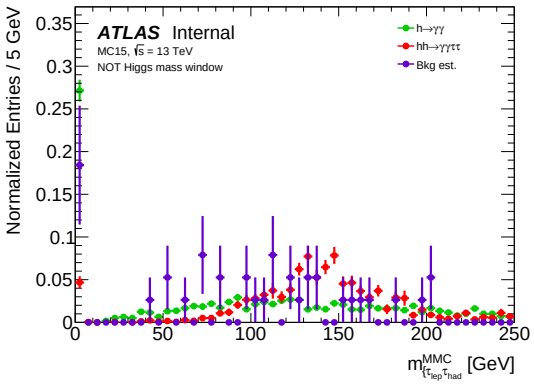

(a) non-resonant

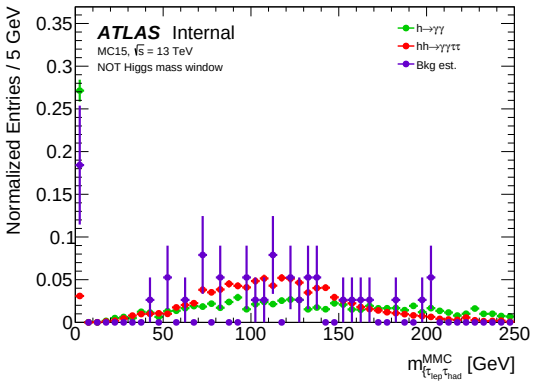

(b) $m_H = 260$

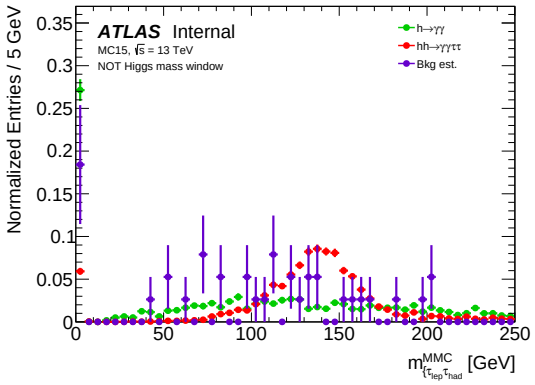

(c) $m_H = 600$

Figure B.10.: $m^{\text{MMC}}_{\tau_{\text{lep}}\tau_{\text{had}}}$ with only the cut on the $m_{\gamma\gamma}$ window applied.

C. Systematic Uncertainties

Table C.1.: Systematic uncertainties on the background MC for the different objects for 30 fb^{-1} for the cuts as applied for the non-resonant di-Higgs production.

Systematic		Variation on event yield [%] Downwards	Upwards
e/γ	overall resolution	0.388	−0.481
	overall scale corr.	1.12	0.626
	scint. scale corr.	-3.68×10^{-6}	3.68×10^{-6}
	LAr calib. scale 2015	−0.117	3.68×10^{-6}
	LAr temp. scale 2015	-3.68×10^{-6}	3.68×10^{-6}
	LAr temp. scale 2016	-3.68×10^{-6}	0.117
Jet	energy range	-3.68×10^{-6}	−0.507
	cal. punch trough	-3.68×10^{-6}	3.68×10^{-6}
	single part.	-3.68×10^{-6}	3.68×10^{-6}
Jet energy scale pile-up	μ	-3.68×10^{-6}	−0.277
	N_{pv}	-3.68×10^{-6}	−0.284
	p_{T} term	-3.68×10^{-6}	0.316
	ρ topology	-3.68×10^{-6}	−0.284
ID eff. for e and μ		-3.68×10^{-6}	3.68×10^{-6}
Luminosity		2.9	2.9
$E_{\text{T}}^{\text{miss}}$ soft term	res. parallel	-3.68×10^{-6}	0.876
	res. perpendicular	-3.68×10^{-6}	−0.808
	scale	−0.164	1.74
Muons	inner detector	-3.68×10^{-6}	3.68×10^{-6}
	muon spectrometer	-3.68×10^{-6}	3.68×10^{-6}
	scale	-3.68×10^{-6}	3.68×10^{-6}
Photon ID eff.		4.59	4.7
Pile-up reweighting	2015	-3.68×10^{-6}	3.68×10^{-6}
	2016	-3.68×10^{-6}	3.68×10^{-6}
τ_{had} ID eff.	high-p_{T}	0.005 66	0.005 67
	total	1.01	1.74
τ_{had} overlap rem. eff.	true electron	0.61	0.61
	true τ_{had}	0.31	0.31
τ_{had} reco. eff.	high-p_{T}	-3.68×10^{-6}	3.68×10^{-6}
	total	1.16	1.16
τ_{had} energy scale	detector	-3.68×10^{-6}	3.68×10^{-6}
	insitu	1.68	0.239
	model	0.152	3.68×10^{-6}
$\sigma \times \text{BR}$		1.1	1.1

Table C.2.: Systematic uncertainties on the non-resonant signal MC for the different objects for $30\,\text{fb}^{-1}$.

Systematic		Variation on event yield [%] Downwards	Upwards
e/γ	overall resolution	-0.629	-0.56
	overall scale corr.	0.287	-1.61
	scint. scale corr.	-0.0896	0.0896
	LAr calib. scale 2015	0.391	-0.14
	LAr temp. scale 2015	-2.27×10^{-6}	2.27×10^{-6}
	LAr temp. scale 2016	-0.153	-0.0363
Jet	energy range	-2.27×10^{-6}	0.0478
	cal. punch trough	0.0215	$-0.002\,42$
	single part.	0.0222	-0.0386
Jet energy scale pile-up	μ	0.0729	-0.0223
	N_{pv}	0.1	-0.0543
	p_{T} term	-2.27×10^{-6}	-4.37×10^{-5}
	ρ topology	-2.27×10^{-6}	2.27×10^{-6}
ID eff. for e and μ		-2.27×10^{-6}	2.27×10^{-6}
Luminosity		2.9	2.9
$E_{\text{T}}^{\text{miss}}$ soft term	res. parallel	-2.27×10^{-6}	-0.299
	res. perpendicular	-2.27×10^{-6}	-0.0857
	scale	-0.0759	-0.197
Muons	inner detector	$-0.000\,852$	0.008 01
	muon spectrometer	-0.0182	0.32
	scale	0.004 62	0.000 699
Photon ID eff.		4.43	4.53
Pile-up reweighting	2015	-2.27×10^{-6}	2.27×10^{-6}
	2016	-2.27×10^{-6}	2.27×10^{-6}
τ_{had} ID eff.	high-p_{T}	0.118	0.118
	total	2.94	5.12
τ_{had} overlap rem. eff.	true electron	$-0.000\,299$	$-0.000\,294$
	true τ_{had}	1.16	1.16
τ_{had} reco. eff.	high-p_{T}	0.0113	0.0114
	total	3.22	3.22
τ_{had} energy scale	detector	0.236	0.0462
	insitu	1.4	0.808
	model	0.278	0.379

Table C.3.: Systematic uncertainties on the resonant signal MC for $m_H = 600\,\text{GeV}$ for $30\,\text{fb}^{-1}$ for the different objects.

Systematic		Variation on event yield [%] Downwards	Upwards
e/γ	overall resolution	-0.352	-0.991
	overall scale corr.	1.29	-0.893
	scint. scale corr.	-0.0226	0.0226
	LAr calib. scale 2015	0.0129	-0.48
	LAr temp. scale 2015	8.64×10^{-7}	-8.64×10^{-7}
	LAr temp. scale 2016	0.0649	-0.176
Jet	energy range	8.64×10^{-7}	-0.139
	cal. punch trough	0.0141	-0.0468
	single part.	-0.026	-0.115
Jet energy scale pile-up	μ	0.102	$-0.002\,04$
	N_{pv}	-0.0409	-0.0872
	p_{T} term	8.64×10^{-7}	-8.64×10^{-7}
	ρ topology	8.64×10^{-7}	-8.64×10^{-7}
ID eff. for e and μ		8.64×10^{-7}	-8.64×10^{-7}
Luminosity		2.9	2.9
$E_{\text{T}}^{\text{miss}}$ soft term	res. parallel	8.64×10^{-7}	-0.168
	res. perpendicular	8.64×10^{-7}	-0.235
	scale	-0.0352	-0.102
Muons	inner detector	0.0278	0.0175
	muon spectrometer	$-0.002\,22$	$-0.000\,522$
	scale	-0.108	-8.64×10^{-7}
Photon ID eff.		4.37	4.47
Pile-up reweighting	2015	8.64×10^{-7}	-8.64×10^{-7}
	2016	8.64×10^{-7}	-8.64×10^{-7}
τ_{had} ID eff.	high-p_{T}	0.196	0.196
	total	3.01	5.21
τ_{had} overlap rem. eff.	true electron	0.002 35	0.002 35
	true τ_{had}	1.2	1.2
τ_{had} reco. eff.	high-p_{T}	0.0209	0.0209
	total	3.03	3.03
τ_{had} energy scale	detector	0.388	0.284
	insitu	1.75	1.06
	model	0.549	0.263

Table C.4.: Systematic uncertainties on the background MC for the different objects for $30\,\text{fb}^{-1}$ for the cuts as applied for the resonant di-Higgs production for $m_H = 260\,\text{GeV}$.

Systematic		Variation on event yield [%] Downwards	Upwards
e/γ	overall resolution	-0.0599	-0.969
	overall scale corr.	0.658	-0.0244
	scint. scale corr.	-6.77×10^{-7}	6.77×10^{-7}
	LAr calib. scale 2015	-0.0721	$-0.001\,72$
	LAr temp. scale 2015	-6.77×10^{-7}	6.77×10^{-7}
	LAr temp. scale 2016	-6.77×10^{-7}	0.0721
Jet	energy range	-6.77×10^{-7}	-0.0583
	cal. punch trough	-6.77×10^{-7}	6.77×10^{-7}
	single part.	-6.77×10^{-7}	6.77×10^{-7}
Jet energy scale pile-up	μ	-6.77×10^{-7}	6.77×10^{-7}
	N_{pv}	-6.77×10^{-7}	6.77×10^{-7}
	p_{T} term	-6.77×10^{-7}	6.77×10^{-7}
	ρ topology	-6.77×10^{-7}	6.77×10^{-7}
ID eff. for e and μ		-6.77×10^{-7}	6.77×10^{-7}
Luminosity		2.9	2.9
$E_{\text{T}}^{\text{miss}}$ soft term	res. parallel	-6.77×10^{-7}	-0.143
	res. perpendicular	-6.77×10^{-7}	-0.407
	scale	-6.77×10^{-7}	6.77×10^{-7}
Muons	inner detector	-6.77×10^{-7}	6.77×10^{-7}
	muon spectrometer	-6.77×10^{-7}	6.77×10^{-7}
	scale	-6.77×10^{-7}	6.77×10^{-7}
Photon ID eff.		4.45	4.55
Pile-up reweighting	2015	-6.77×10^{-7}	6.77×10^{-7}
	2016	-6.77×10^{-7}	6.77×10^{-7}
τ_{had} ID eff.	high-p_{T}	0.004 45	0.004 46
	total	0.765	1.31
τ_{had} overlap rem. eff.	true electron	0.554	0.554
	true τ_{had}	0.226	0.226
τ_{had} reco. eff.	high-p_{T}	-6.77×10^{-7}	6.77×10^{-7}
	total	0.879	0.879
τ_{had} energy scale	detector	-6.77×10^{-7}	6.77×10^{-7}
	insitu	1.03	0.147
	model	0.0933	6.77×10^{-7}
$\sigma \times \text{BR}$		1.1	1.1

Table C.5.: Systematic uncertainties on the resonant signal MC for $m_H = 260\,\text{GeV}$ for $30\,\text{fb}^{-1}$ for the different objects.

Systematic		Variation on event yield [%] Downwards	Upwards
e/γ	overall resolution	-0.527	-0.642
	overall scale corr.	0.886	-0.869
	scint. scale corr.	0.0141	-0.0141
	LAr calib. scale 2015	0.0179	0.0856
	LAr temp. scale 2015	-3.78×10^{-6}	3.78×10^{-6}
	LAr temp. scale 2016	-0.0804	0.111
Jet	energy range	-3.78×10^{-6}	-0.982
	cal. punch trough	0.0321	-0.0992
	single part.	0.0042	-0.299
Jet energy scale pile-up	μ	0.0278	-0.0707
	N_{pv}	-0.302	-0.313
	p_{T} term	-3.78×10^{-6}	3.78×10^{-6}
	ρ topology	-3.78×10^{-6}	3.78×10^{-6}
ID eff. for e and μ		-3.78×10^{-6}	3.78×10^{-6}
Luminosity		2.9	2.9
$E_{\text{T}}^{\text{miss}}$ soft term	res. parallel	-3.78×10^{-6}	-0.83
	res. perpendicular	-3.78×10^{-6}	-0.395
	scale	-0.27	-0.277
Muons	inner detector	-0.0341	0.004 54
	muon spectrometer	-0.0149	0.0393
	scale	-0.0034	3.78×10^{-6}
Photon ID eff.		4.52	4.62
Pile-up reweighting	2015	-3.78×10^{-6}	3.78×10^{-6}
	2016	-3.78×10^{-6}	3.78×10^{-6}
τ_{had} ID eff.	high-p_{T}	4.48×10^{-5}	5.24×10^{-5}
	total	3.02	5.22
τ_{had} overlap rem. eff.	true electron	-3.78×10^{-6}	3.78×10^{-6}
	true τ_{had}	0.922	0.922
τ_{had} reco. eff.	high-p_{T}	-3.78×10^{-6}	3.78×10^{-6}
	total	3.76	3.76
τ_{had} energy scale	detector	-0.496	0.0291
	insitu	1.83	0.698
	model	0.341	0.579

D. Joboptions for the Resonant Signal Monte Carlo

Listing D.1: Common joboption for resonant di-Higgs production.

```
# joboption for Double Higgs production (h1 h1) in gluon-fusion, with top-quark
# mass effects, in the 2HDM (arXiv:1407.0281)

from MadGraphControl.MadGraphUtils import *
import tarfile, shutil, os, glob

cwd = os.getcwd()

mode=0

run_number = runArgs.runNumber
if (run_number > run_number_max):
    log.fatal('Run number out of validity range for this generation.'
            'run_number_max '+str(run_number_max))
    raise RunTimeError('Run number too high.')

imass = run_number - run_number_min + offset

# Extract files for the job
ggh1h1_NLO = tarfile.open(runArgs.inputGenConfFile)
ggh1h1_NLO.extractall()
ggh1h1_NLO.close()

def numbers_to_mass(argument):
    switcher = {  0:  260.,
                  1:  275.,
                  2:  300.,
                  3:  325.,
                  4:  350.,
                  5:  400.,
                  6:  450.,
                  7:  500.,
                  8:  600.,
                  9:  700.,
                 10:  750.,
                 11:  800.,
                 12:  900.,
                 13: 1000.,
```

```
                  14: 1100.,
                  15: 1200.,
                  16: 1300.,
                  17: 1400.,
                  18: 1500.,
                  19: 1600.,
                  20: 1800.,
                  21: 2000.,
                  22: 2250.,
                  23: 2500.,
                  24: 2750.,
                  25: 3000.,
                  26: 3250.,
                  27: 3500.,
                  28: 3750.,
                  29: 4000.,
                  30: 4500.,
                  31: 5000. }

    return switcher.get(argument, "nothing")

# Setting higgs masses
m_h2 = numbers_to_mass(imass)
higgsMasses = { 'm_h1' : '1.250900e+02',
                'm_h2' : str(m_h2) }

# Setting decay widths
decays = { 'Wh2' : '1.000000e-03' }

# Setting renormalisation scale in param_card
scale = m_h2 / 2.
loop = { 'MU_R' : str(scale) }
parameters = { 'decay' : decays,
               'loop' : loop,
               'mass' : higgsMasses }

# setting some parameters for run_card.dat
extras = { 'lhe_version' : '3.0',
           'pdlabel' : 'lhapdf',
           'lhaid' : '11000',
           'PDF_set_min': '11001',
           'PDF_set_max': '11052',
           'parton_shower' : 'HERWIGPP',
           'muR_ref_fixed' : str(scale),
           'muF1_ref_fixed' : str(scale),
           'muF2_ref_fixed' : str(scale),
           'QES_ref_fixed' : str(scale) }

# Generating di-higgs through Heavy Higgs resonance with MadGraph
fcard = open('proc_card_mg5.dat','w')
fcard.write("""
set group_subprocesses Auto
set ignore_six_quark_processes False
set loop_optimized_output True
```

```
set complex_mass_scheme False
import model sm
define p = g u c d s u~ c~ d~ s~
define j = g u c d s u~ c~ d~ s~
define l+ = e+ mu+
define l- = e- mu-
define vl = ve vm vt
define vl~ = ve~ vm~ vt~
import model 2HDMCP_EFT
generate p p > h1 h1 [real=QCD]
output""")
fcard.close()

beamEnergy = -999
if hasattr(runArgs,'ecmEnergy'):
    beamEnergy = runArgs.ecmEnergy / 2.
else:
    raise RuntimeError("No center of mass energy found.")

# Setting the number of events and add protection to avoid crashing with
# maxEvents=-1
nevents = 5000 * safefactor
if evgenConfig.minevents > 0 :
   nevents = evgenConfig.minevents * safefactor

if runArgs.maxEvents > 0:
    nevents = runArgs.maxEvents * safefactor

# Using the helper function from MadGraphControl for setting up the run_card
# Build a new run_card.dat from an existing one
# Using the values given in "extras" above for the selected parameters when
# setting up the run_card
# If not set in "extras", default values are used
build_run_card(run_card_old='run_card.template.dat',
        run_card_new='run_card.dat', nevts=nevents,
        rand_seed=runArgs.randomSeed, beamEnergy=beamEnergy, extras=extras,
        xqcut=0.0)

# Using the helper function from MadGraphControl for setting up the param_card
# Build a new param_card.dat from an existing one
# Higgs masses are set by 'higgsMasses'
build_param_card(param_card_old='param_card.dat',
        param_card_new='param_card_new.dat', params=parameters)

print_cards()

runName='run_01'

process_dir = 'PROCNLO_2HDMCP_EFT_0'

# fetch and compile additional files
shutil.copytree(os.environ['MADPATH'] + '/vendor/CutTools', 'vendors/CutTools')
shutil.copytree(os.environ['MADPATH'] + '/vendor/StdHEP', 'vendors/StdHEP')
shutil.copytree(os.environ['MADPATH'] + '/vendor/IREGI', 'vendors/IREGI')
```

```
os.chdir(cwd + '/vendors/CutTools')
os.system('make clean && make -j1')
os.chdir(cwd + '/vendors/StdHEP')
os.system('make clean && make -j1')
os.chdir(cwd + '/vendors/IREGI/src')
os.system('make clean && make')
os.chdir(cwd + '/code/Source/DHELAS')
os.system('make clean && make')
os.chdir(cwd + '/code/Source/MODEL')
os.system('make clean && make')
os.chdir(cwd + '/code/SubProcesses/P0_gg_h1h1')
os.system('make clean && make reweight_FT4')
os.chdir(cwd + '/code/SubProcesses/P1_gg_h1h1g')
os.system('make clean && make reweight_FT4')
os.chdir(cwd + '/code/SubProcesses/P2_ug_h1h1u')
os.system('make clean && make reweight_FT4')
os.chdir(cwd)

# generate the events
generate(run_card_loc='run_card.dat', param_card_loc='param_card_new.dat',
        mode=mode, proc_dir=process_dir, run_name=runName)

# do the reweighting
os.chdir(cwd + '/' + process_dir + '/Events/' + runName)
os.system('gunzip events.lhe.gz')

#first step, reweight the S events
os.chdir(cwd + '/code/SubProcesses/P0_gg_h1h1')
shutil.copy(cwd + '/' + process_dir + '/Events/' + runName + '/events.lhe', '.')
os.system('echo -e events.lhe "\n 1\n"  | ./reweight_FT4')

#second step, reweight the gg H events
os.chdir(cwd + '/code/SubProcesses/P1_gg_h1h1g')
shutil.copy(cwd + '/code/SubProcesses/P0_gg_h1h1/events.lhe.rwgt1', '.')
os.system('echo -e events.lhe.rwgt1 "\n 1\n"  | ./reweight_FT4')
os.remove('events.lhe.rwgt1')

#third step, reweight the qq H events
os.chdir(cwd + '/code/SubProcesses/P2_ug_h1h1u')
shutil.copy(cwd + '/code/SubProcesses/P1_gg_h1h1g/events.lhe.rwgt1.rwgt2', '.')
os.system('echo -e events.lhe.rwgt1.rwgt2 "\n 1\n"  | ./reweight_FT4')
os.remove('events.lhe.rwgt1.rwgt2')

#finally compute scale and PDF uncertainties
os.chdir(cwd + '/' +process_dir + '/SubProcesses/P0_gg_h1h1/')
shutil.copy(cwd +
        '/code/SubProcesses/P2_ug_h1h1u/events.lhe.rwgt1.rwgt2.rwgt3', '.')
os.system('echo -e events.lhe.rwgt1.rwgt2.rwgt3 "\n 1\n"  |
        ./reweight_xsec_events')
os.remove('events.lhe.rwgt1.rwgt2.rwgt3')

shutil.move('events.lhe.rwgt1.rwgt2.rwgt3.rwgt', 'events.lhe.rwgt')

os.chdir(cwd + '/' +process_dir + '/Events/' + runName)
```

```
shutil.copy(cwd + '/' +process_dir +
        '/SubProcesses/P0_gg_h1h1/events.lhe.rwgt', '.')

# calculate xsec
os.chdir(cwd + '/' + process_dir + '/Events/' + runName)
shutil.move(cwd + '/' + process_dir + '/SubProcesses/P0_gg_h1h1/rwgt.dat', '.')
shutil.copy(cwd + '/' + process_dir + '/Events/xsec.py', '.')
os.system('python xsec.py > xsec_after_reweighting.dat')
os.system('python xsec.py')

# finalise and cleanup cruft
os.chdir(cwd + '/' + process_dir + '/Events/' + runName)
os.system('rename .lhe .lhe.before_rwgt *.lhe')
os.system('rename .lhe.rwgt .lhe *.lhe.rwgt')
os.remove(cwd + '/' + process_dir + '/SubProcesses/P0_gg_h1h1/events.lhe.rwgt')
os.chdir(cwd + '/code/SubProcesses/P0_gg_h1h1')
for file in glob.glob("events*"):
    os.remove(file)
os.chdir(cwd + '/code/SubProcesses/P1_gg_h1h1g/')
for file in glob.glob("events*"):
    os.remove(file)
os.chdir(cwd + '/code/SubProcesses/P2_ug_h1h1u/')
for file in glob.glob("events*"):
    os.remove(file)

os.chdir(cwd + '/' + process_dir + '/Events/' + runName)
os.system('gzip events.lhe')
os.chdir(cwd)

arrange_output(run_name=runName, proc_dir=process_dir,
        outputDS=runName+'._00001.events.tar.gz')

#--------------------------------------------------------------
# Showering with HerwigPP, UE-EE-5 tune
#--------------------------------------------------------------
include("MC15JobOptions/Herwigpp_UEEE5_CTEQ6L1_CT10ME_LHEF_EvtGen_Common.py")
## To modify Higgs BR
cmds = """
create ThePEG::ParticleData h2
setup h2 35  h2 """
cmds += str(m_h2)
cmds += """ 1.0 10.0 1.973269631e-13 2 3 2 0
set /Herwig/EventHandlers/LHEReader:AllowedToReOpen 0
set /Herwig/Shower/KinematicsReconstructor:ReconstructionOption General
set /Herwig/Shower/KinematicsReconstructor:InitialInitialBoostOption LongTransBoost
"""

from Herwigpp_i import config as hw
genSeq.Herwigpp.Commands += cmds.splitlines()
genSeq.Herwigpp.Commands += cmdsps.splitlines()
del cmds
del cmdsps

#--------------------------------------------------------------------------------
```

```
# EVGEN Configuration
#--------------------------------------------------------------------------------
evgenConfig.generators += ["aMcAtNlo", "Herwigpp"]
evgenConfig.description += ", h2 is a " +str(m_h2)+ " scalar."

evgenConfig.contact = ['Biagio Di Micco <biagio.di.micco@cern.ch>',
        'Julian Wollrath <wollrath@cern.ch>']

evgenConfig.inputfilecheck = runName
runArgs.inputGeneratorFile=runName+'._00001.events.tar.gz'
```

Listing D.2: Joboption for the resonant signal MC for $m_H = 260\,\text{GeV}$.

```
from MadGraphControl.MadGraphUtils import *

mode = 0

cmdsps = """set /Herwig/Particles/h0:Width_generator NULL
set /Herwig/Particles/h0:Mass_generator NULL
do /Herwig/Particles/h0:SelectDecayModes h0->tau-,tau+; h0->gamma,gamma;
set /Herwig/Particles/h0/h0->tau-,tau+;:BranchingRatio  0.5
set /Herwig/Particles/h0/h0->gamma,gamma;:BranchingRatio  0.5
"""
safefactor = 7
evgenConfig.description = "h2->h1h1 diHiggs production with MG5_aMC@NLO, h1 ->"
evgenConfig.description += " yy,tautau yytt  lep had"
evgenConfig.keywords = ["BSM",  "BSMHiggs", "resonance", "tau"]

run_number_min = 343804
run_number_max = 343817
offset = 0

include("MC15JobOptions/MadGraphControl_HerwigppEvtGen_UEEE5_CT10ME_NLO_h2h1h1.py")

#--------------------------------------------------------------------------------
# Generator Filters
#--------------------------------------------------------------------------------
from GeneratorFilters.GeneratorFiltersConf import ParentChildFilter
filtSeq += ParentChildFilter("hyyFilter", PDGParent = [25], PDGChild = [22])
filtSeq += ParentChildFilter("hTauTauFilter", PDGParent = [25], PDGChild = [15])
include("MC15JobOptions/XtoVVDecayFilterExtended.py")
filtSeq.XtoVVDecayFilterExtended.PDGGrandParent = 25
filtSeq.XtoVVDecayFilterExtended.PDGParent = 15
filtSeq.XtoVVDecayFilterExtended.StatusParent = 2
filtSeq.XtoVVDecayFilterExtended.PDGChild1 = [11, 13]
filtSeq.XtoVVDecayFilterExtended.PDGChild2 = [24, 211, 213, 215, 311, 321,
        323, 10232, 10323, 20213, 20232, 20323, 30213, 100213, 100323, 1000213]
filtSeq.Expression = "hyyFilter and hTauTauFilter and XtoVVDecayFilterExtended"

evgenConfig.generators  = ["aMcAtNlo", "Herwigpp", "EvtGen"]
```

Bibliography

[1] K. A. Olive, et al. (Particle Data Group), *Review of Particle Physics*, Chin. Phys. **C38**, 090001 (2014)

[2] S. L. Glashow, *Partial Symmetries of Weak Interactions*, Nucl. Phys. **22**, 579 (1961)

[3] A. Salam, *Weak and Electromagnetic Interactions*, Conf. Proc. **C680519**, 367 (1968)

[4] S. Weinberg, *A Model of Leptons*, Phys. Rev. Lett. **19**, 1264 (1967)

[5] P. W. Higgs, *Broken Symmetries and the Masses of Gauge Bosons*, Phys. Rev. Lett. **13**, 508 (1964)

[6] F. Englert, R. Brout, *Broken Symmetry and the Mass of Gauge Vector Mesons*, Phys. Rev. Lett. **13**, 321 (1964)

[7] G. Aad, et al. (ATLAS), *Observation of a new particle in the search for the Standard Model Higgs boson with the ATLAS detector at the LHC*, Phys. Lett. **B716**, 1 (2012), 1207.7214

[8] S. Chatrchyan, et al. (CMS), *Observation of a new boson at a mass of 125 GeV with the CMS experiment at the LHC*, Phys. Lett. **B716**, 30 (2012), 1207.7235

[9] G. Aad, et al. (ATLAS, CMS), *Combined Measurement of the Higgs Boson Mass in pp Collisions at $\sqrt{s} = 7$ and 8 TeV with the ATLAS and CMS Experiments*, Phys. Rev. Lett. **114**, 191803 (2015), 1503.07589

[10] G. Aad, et al. (ATLAS), *Measurement of Higgs boson production in the diphoton decay channel in pp collisions at center-of-mass energies of 7 and 8 TeV with the ATLAS detector*, Phys. Rev. **D90(11)**, 112015 (2014), 1408.7084

[11] V. Khachatryan, et al. (CMS), *Observation of the diphoton decay of the Higgs boson and measurement of its properties*, Eur. Phys. J. **C74(10)**, 3076 (2014), 1407.0558

[12] G. Aad, et al. (ATLAS), *Evidence for the Higgs-boson Yukawa coupling to tau leptons with the ATLAS detector*, JHEP **04**, 117 (2015), 1501.04943

[13] S. Chatrchyan, et al. (CMS), *Evidence for the 125 GeV Higgs boson decaying to a pair of τ leptons*, JHEP **05**, 104 (2014), 1401.5041

[14] S. Heinemeyer, et al. (LHC Higgs Cross Section Working Group), *Handbook of LHC Higgs Cross Sections: 3. Higgs Properties: Report of the LHC Higgs Cross Section Working Group*, Technical Report arXiv:1307.1347. CERN-2013-004, Geneva (2013), comments: 404 pages, 139 figures, to be submitted to CERN Report. Working Group web page: https://twiki.cern.ch/twiki/bin/view/LHCPhysics/CrossSections, URL https://cds.cern.ch/record/1559921

[15] ATLAS Collaboration, *Summary of several Standard Model total and fiducial production cross section measurements* (2016), URL https://atlas.web.cern.ch/Atlas/GROUPS/PHYSICS/CombinedSummaryPlots/SM/

[16] Z. Maki, M. Nakagawa, S. Sakata, *Remarks on the unified model of elementary particles*, in *High-energy physics. Proceedings, 11th International Conference, ICHEP'62, Geneva, Switzerland, Jul 4-11, 1962*, pages 663–666 (1962), URL https://inspirehep.net/record/1341897/files/C62-07-04-p663.pdf

[17] M. B. Gavela, P. Hernandez, J. Orloff, O. Pene, *Standard model CP violation and baryon asymmetry*, Mod. Phys. Lett. **A9**, 795 (1994), hep-ph/9312215

[18] G. Bertone, D. Hooper, J. Silk, *Particle dark matter: Evidence, candidates and constraints*, Phys. Rept. **405**, 279 (2005), hep-ph/0404175

[19] T. D. Lee, *A Theory of Spontaneous T Violation*, Phys. Rev. **D8**, 1226 (1973)

[20] R. D. Peccei, H. R. Quinn, *CP Conservation in the Presence of Pseudoparticles*, Phys. Rev. Lett. **38**, 1440 (1977)

[21] G. C. Branco, et al., *Theory and phenomenology of two-Higgs-doublet models*, Phys. Rept. **516**, 1 (2012), 1106.0034

[22] M. J. Dolan, C. Englert, M. Spannowsky, *Higgs self-coupling measurements at the LHC*, JHEP **10**, 112 (2012), 1206.5001

[23] V. Barger, et al., *Higgs-Pair Production and Measurement of the Triscalar Coupling at LHC(8,14)*, Phys. Lett. **B728**, 433 (2014), 1311.2931

[24] G. Aad, et al. (ATLAS), *Searches for Higgs boson pair production in the hh $\rightarrow$ bb$\tau\tau$, $\gamma\gamma WW^*$, $\gamma\gamma$bb, bbbb channels with the ATLAS detector*, Phys. Rev. **D92**, 092004 (2015), 1509.04670

[25] D. E. De Florian Sabaris, et al., *Handbook of LHC Higgs cross sections: 4. Deciphering the nature of the Higgs sector* (2016), URL https://cds.cern.ch/record/2215893

[26] O. S. Brüning, et al., *LHC Design Report*, CERN, Geneva (2004), URL https://cds.cern.ch/record/782076

[27] C. De Melis, *The CERN accelerator complex. Complexe des accélérateurs du CERN* (2016), URL https://cds.cern.ch/record/2119882

[28] A. Airapetian, et al. (ATLAS Collaboration), *ATLAS detector and physics performance: Technical Design Report, 1*, Technical Design Report ATLAS, CERN, Geneva (1999), URL https://cds.cern.ch/record/391176

[29] G. L. Bayatian, et al. (CMS), *CMS physics: Technical design report* (2006)

[30] LHCb Collaboration, *LHCb technical design report: Reoptimized detector design and performance* (2003)

[31] F. Piuz, et al. (ALICE Collaboration), *ALICE high-momentum particle identification: Technical Design Report*, Technical Design Report ALICE, CERN, Geneva (1998), URL https://cds.cern.ch/record/381431

[32] V. Berardi, et al. (TOTEM), *TOTEM: Technical design report. Total cross section, elastic scattering and diffraction dissociation at the Large Hadron Collider at CERN* (2004)

[33] O. Adriani, et al. (LHCf), *Technical design report of the LHCf experiment: Measurement of photons and neutral pions in the very forward region of LHC* (2006)

[34] J. Pinfold, et al. (MoEDAL), *Technical Design Report of the MoEDAL Experiment* (2009)

[35] J. Pequenao, *Computer generated image of the whole ATLAS detector* (2008), URL `https://cds.cern.ch/record/1095924`

[36] ATLAS Collaboration (ATLAS), *ATLAS magnet system: Technical design report* (1997)

[37] ATLAS Collaboration (ATLAS), *ATLAS inner detector: Technical design report. Vol. 1* (1997)

[38] ATLAS Collaboration (ATLAS), *ATLAS inner detector: Technical design report. Vol. 2* (1997)

[39] M. Capeans, et al., *ATLAS Insertable B-Layer Technical Design Report*, Technical Report CERN-LHCC-2010-013. ATLAS-TDR-19 (2010), URL `https://cds.cern.ch/record/1291633`

[40] ATLAS Collaboration (ATLAS), *ATLAS liquid argon calorimeter: Technical design report* (1996)

[41] ATLAS Collaboration (ATLAS), *ATLAS tile calorimeter: Technical design report* (1996)

[42] ATLAS Collaboration (ATLAS), *ATLAS muon spectrometer: Technical design report* (1997)

[43] Y. Nakahama, *The ATLAS Trigger System: Ready for Run-2*, J. Phys. Conf. Ser. **664(8)**, 082037 (2015)

[44] S. Agostinelli, et al. (GEANT4), *GEANT4: A Simulation toolkit*, Nucl. Instrum. Meth. **A506**, 250 (2003)

[45] T. Sjostrand, S. Mrenna, P. Z. Skands, *A Brief Introduction to PYTHIA 8.1*, Comput. Phys. Commun. **178**, 852 (2008), `0710.3820`

[46] P. Nason, *A New method for combining NLO QCD with shower Monte Carlo algorithms*, JHEP **11**, 040 (2004), `hep-ph/0409146`

[47] H.-L. Lai, M. Guzzi, J. Huston, Z. Li, P. M. Nadolsky, J. Pumplin, C. P. Yuan, *New parton distributions for collider physics*, Phys. Rev. **D82**, 074024 (2010), 1007.2241

[48] G. Aad, et al. (ATLAS), *Measurement of the Z/γ^* boson transverse momentum distribution in pp collisions at $\sqrt{s}$ = 7 TeV with the ATLAS detector*, JHEP **09**, 145 (2014), 1406.3660

[49] R. D. Ball, et al., *Parton distributions with LHC data*, Nucl. Phys. **B867**, 244 (2013), 1207.1303

[50] ATLAS Collaboration, *ATLAS Run 1 Pythia8 tunes*, Technical Report ATL-PHYS-PUB-2014-021, CERN, Geneva (2014), URL https://cds.cern.ch/record/1966419

[51] J. Alwall, et al., *The automated computation of tree-level and next-to-leading order differential cross sections, and their matching to parton shower simulations*, JHEP **07**, 079 (2014), 1405.0301

[52] M. Bahr, et al., *Herwig++ Physics and Manual*, Eur. Phys. J. **C58**, 639 (2008), 0803.0883

[53] B. Hespel, D. Lopez-Val, E. Vryonidou, *Higgs pair production via gluon fusion in the Two-Higgs-Doublet Model*, JHEP **09**, 124 (2014), 1407.0281

[54] ATLAS Collaboration, *Expected electron performance in the ATLAS experiment*, Technical Report ATL-PHYS-PUB-2011-006, CERN, Geneva (2011)

[55] G. Aad, et al. (ATLAS), *Muon reconstruction performance of the ATLAS detector in proton–proton collision data at $\sqrt{s}$ =13 TeV*, Eur. Phys. J. **C76(5)**, 292 (2016), 1603.05598

[56] M. Cacciari, G. P. Salam, G. Soyez, *The Anti-k(t) jet clustering algorithm*, JHEP **04**, 063 (2008), 0802.1189

[57] *Reconstruction, Energy Calibration, and Identification of Hadronically Decaying Tau Leptons in the ATLAS Experiment for Run-2 of the LHC*, Technical Report ATL-PHYS-PUB-2015-045, CERN, Geneva (2015), URL https://cds.cern.ch/record/2064383

[58] ATLAS Collaboration, *Expected photon performance in the ATLAS experiment*, Technical Report ATL-PHYS-PUB-2011-007, CERN, Geneva (2011)

[59] G. Aad, et al. (ATLAS), *Performance of algorithms that reconstruct missing transverse momentum in $\sqrt{s} = 8$ TeV proton-proton collisions in the ATLAS detector* (2016), 1609.09324

[60] R. K. Ellis, I. Hinchliffe, M. Soldate, J. J. van der Bij, *Higgs Decay to tau+ tau-: A Possible Signature of Intermediate Mass Higgs Bosons at the SSC*, Nucl. Phys. **B297**, 221 (1988)

[61] A. Elagin, et al., *A New Mass Reconstruction Technique for Resonances Decaying to di-tau*, Nucl. Instrum. Meth. **A654**, 481 (2011), 1012.4686

[62] G. Cowan, E. Gross, *Discovery significance with statistical uncertainty in the background estimate* (2008), ATLAS Statistics Forum, URL https://www.pp.rhul.ac.uk/ cowan/stat/notes/SigCalcNote.pdf

[63] M. Aaboud, et al. (ATLAS), *Luminosity determination in pp collisions at $\sqrt{s}$ = 8 TeV using the ATLAS detector at the LHC* (2016), 1608.03953

[64] K. Cranmer, et al. (ROOT Collaboration), *HistFactory: A tool for creating statistical models for use with RooFit and RooStats*, Technical Report CERN-OPEN-2012-016, New York U., New York (2012), URL https://cds.cern.ch/record/1456844

[65] M. Baak, et al., *HistFitter software framework for statistical data analysis*, Eur. Phys. J. **C75**, 153 (2015), 1410.1280

[66] T. Junk, *Confidence level computation for combining searches with small statistics*, Nucl. Instrum. Meth. **A434**, 435 (1999), hep-ex/9902006

[67] A. L. Read, *Modified frequentist analysis of search results (the CL_s method)* **(CERN-OPEN-2000-205)** (2000), URL https://cds.cern.ch/record/451614

Erklärung nach §17(9) der Prüfungsordnung für den Bachelor-Studiengang Physik und den Master-Studiengang Physik an der Universität Göttingen:

Hiermit erkläre ich, dass ich diese Abschlussarbeit selbständig verfasst habe, keine anderen als die angegebenen Quellen und Hilfsmittel benutzt habe und alle Stellen, die wörtlich oder sinngemäß aus veröffentlichten Schriften entnommen wurden, als solche kenntlich gemacht habe.
Darüberhinaus erkläre ich, dass diese Abschlussarbeit nicht, auch nicht auszugsweise, im Rahmen einer nichtbestandenen Prüfung an dieser oder einer anderen Hochschule eingereicht wurde.

Göttingen, den 10. Oktober 2016

(Julian Wollrath)